UniUGG: Unified 3D Understanding and Generation via Geometric-Semantic Encoding

Anonymous authors
Paper under double-blind review

Abstract

Despite the impressive progress on understanding and generating images shown by the recent unified architectures, the integration of 3D tasks remains challenging and largely unexplored. In this paper, we introduce *UniUGG*, the first unified understanding and generation framework for 3D modalities. Our unified framework employs an LLM to comprehend and decode sentences and 3D representations. At its core, we propose a spatial decoder leveraging a latent diffusion model to generate high-quality 3D representations. This allows for the generation and imagination of 3D scenes based on a reference image and an arbitrary view transformation, while remaining supports for spatial visual question answering (VQA) tasks. Additionally, we propose a geometric-semantic learning strategy to pretrain the vision encoder. This design jointly captures the input's semantic and geometric cues, enhancing both spatial understanding and generation. Extensive experimental results demonstrate the superiority of our method in visual representation, spatial understanding, and 3D generation.

1 Introduction

Recent work on unified 2D understanding and generation has made significant strides (Sun et al., 2023; 2024; Ye et al., 2024; Dong et al., 2024; Wu et al., 2024; Team, 2024; Wang et al., 2024a; Liu et al., 2024a; Wu et al., 2025; Chen et al., 2025; Huang et al., 2025). Early works (Sun et al., 2023; 2024; Ye et al., 2024; Dong et al., 2024) build unified frameworks that couple an autoregressive LLM with a diffusion image decoder. The LLM consumes text–vision inputs and produces a fixed set of learnable queries whose features are regressed into the diffusion latent space; the diffusion model then synthesizes the image conditioned on these latents. Subsequent works (Team, 2024; Liu et al., 2024a; Wu et al., 2024) employ VQ tokenizers for the unified generation of texts and images.

Although the aforementioned works have made significant progress in images, the challenge of achieving unified understanding and generation for 3D modalities remains largely unexplored. Several benchmarks (Zhang et al., 2025b; Fu et al., 2024b; Ma et al., 2024; Yang et al., 2025) integrate large-scale public datasets and design spatial VQA tasks to enhance the spatial reasoning capability of LLMs. However, these efforts focus solely on spatial understanding and take a rather brute-force approach—directly fine-tuning LLMs with large amounts of spatial data, which has shown limited effectiveness. Other works (Chen et al., 2024a; Cheng et al., 2024; Hong et al., 2023; Driess et al., 2023; Chen et al., 2024e; Zhu et al., 2024a) incorporate additional modalities, such as depth, point clouds, or scene graphs, to handle spatial understanding. Unfortunately, these methods introduce additional disadvantages, as they often require specialized data acquisition devices or necessitate explicit spatial modeling of the entire scene. These drawbacks hinder potential development for practical applications.

We identify two main challenges that bottleneck progress for the unified 3D frameworks. **The first issue is the limitation of visual representations.** Current LLMs typically rely on vision encoders pretrained on 2D image semantic tasks, which lack the capability to model 3D geometries. This limitation creates a performance bottleneck, particularly in spatial understanding tasks. **The second issue is the incompatibility between 3D generation and LLMs.** Here, LLMs are built on the basis of tokenization methods to autoregressively generate the next token. This scheme adapts well to image generation, as images are regular and can be tokenized into a fixed number of elements. However, such tokenization approaches are not easily applicable to 3D data such as point clouds due

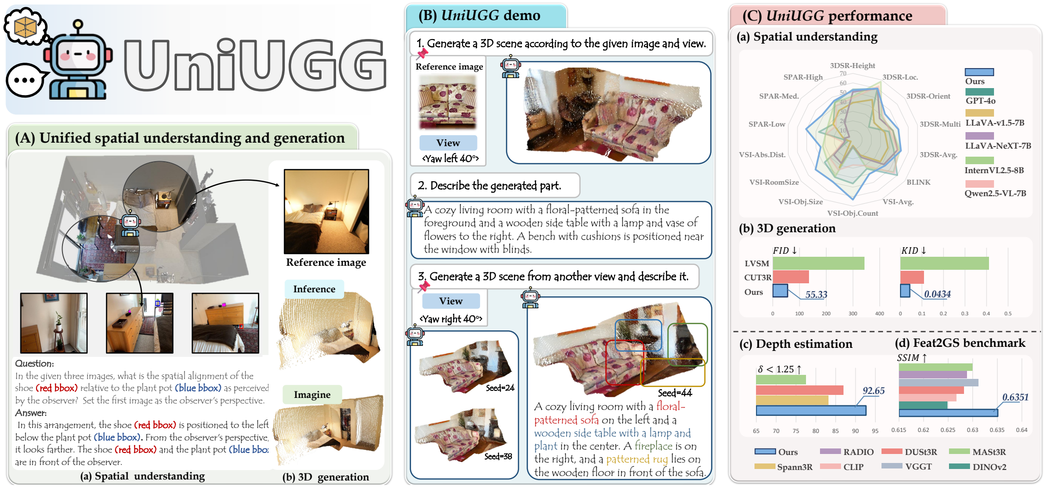

Question:
In the given three images, what is the spatial alignment of the shoe (red bbox) relative to the plant pot (blue bbox) as perceived by the observer? Set the first image as the observer's perspective.
Answer:
In this arrangement, the shoe (red bbox) is positioned to the left below the plant pot (blue bbox). From the observer's perspective, it looks farther. The shoe (red bbox) and the plant pot (blue bbo: are in front of the observer.

1. Generate a 3D scene according to the given image and view.

2. Describe the generated part.

A cozy living room with a floral-patterned sofa in the foreground and a wooden side table with a lamp and vase of flowers to the right. A bench with cushions is positioned near the window with blinds.

3. Generate a 3D scene from another view and describe it.

A cozy living room with a floral-patterned sofa on the left and a wooden side table with a lamp and plant in the center. A fireplace is on the right, and a patterned rug lies on the wooden floor in front of the sofa.

Figure 1: **We introduce *UniUGG*, the first unified framework for spatial understanding and generation.** (A) *UniUGG* supports spatial-level VQA and generates geometrically consistent 3D scenes. (B) Given a reference image, it can creatively generate 3D variations and describe them accurately. (C) *UniUGG* outperforms baselines in both spatial understanding and generation, with our specially tuned vision encoder excelling in downstream tasks.

to the irregular nature of representations. This tokenization gap makes it more challenging for LLMs to handle autoregressive 3D generation tasks effectively.

Recently, a line of works (Wang & Agapito, 2024; Leroy et al., 2024; Zhang et al., 2024; Wang et al., 2025b;a) initiated by DUSt3R (Wang et al., 2024b) have introduced a new perspective on spatial representation by aligning pixels across multi-view into a unified global coordinate system. The multi-view geometry training paradigm enables models to reconstruct 3D scenes from visual inputs, along with predicting spatial relationships. Inspired by this, we introduce *UniUGG*, the first framework for unified spatial understanding and generation, marking a significant step by solving the aforementioned two issues.

For the first issue, we design a geometric-semantic learning strategy for vision encoder pretraining. This strategy incorporates semantic information from a teacher model while integrating the encoder with a spatial decoder for end-to-end multi-view geometric training, thereby enhancing its spatial modeling capabilities. The resulting ViT representations significantly improve both understanding and generation within the unified framework and yield better results in a variety of downstream tasks. The learning strategy not only provides the LLM with an enriched representation but also bridges the gap between vision and 3D using the spatial decoder. This decoder, a byproduct of the pretraining process, decodes visual representations into 3D scenes corresponding to the two inputs. Upon these, we solve the second issue by designing *UniUGG*. *UniUGG* takes a reference visual representation and an encoded target-view raymap as input, producing conditional features. These features are then used with a diffusion model to generate the visual representation of the target-view. To enhance this process, we design the Spatial-VAE, which effectively compresses geometric-semantic information, enabling more accurate and efficient representation generation. Additionally, it links the spatial decoder for end-to-end fine-tuning, enhancing information compression while mitigating the negative impact of discrepancies between the reconstructed and original representations on 3D scene decoding. Finally, both the original and generated visual representations are passed through the fine-tuned spatial decoder to decode the 3D scene. Thanks to the LLM-based architecture, *UniUGG* simultaneously learn understanding and generation tasks, enabling its 3D scene inference, while maintaining spatial VQA capabilities for both real and generated representations.

Our main **contributions** are summarized as follows: **(i)** We propose the first LLM-based unified generation and understanding framework for 3D scenes, *UniUGG*, which enables spatial-level VQA and generates geometrically consistent rich 3D environments. **(ii)** We introduce a novel geometric-semantic vision encoder pretraining strategy. Here, our ViT encodes geometric cues from input image pairs and preserves semantic features from 2D priors. **(iii)** We present a Spatial-VAE as the core of our 3D scene representation generation scheme. Our Spatial-VAE compresses the 3D geometric-semantic representations from input image pairs and helps producing sharper 3D point clouds as output. **(iv)** Our method achieves top performance on multiple spatial reasoning benchmarks, surpassing baselines on VSI-Bench by 17.9% in particular, and maintaining significant superiority in 3D generation.

2 Related works

Language models for spatial reasoning and generation There has been growing interest in applying large multimodal language models to spatial reasoning tasks. Recent models (Alayrac et al., 2022; Driess et al., 2023; Liu et al., 2023; Li et al., 2024a; Bai et al., 2023) have shown impressive results in language-guided visual understanding, but they often focus primarily on semantic alignment. As a result, they exhibit clear limitations when it comes to understanding spatial relations, viewpoint changes, and structural consistency. Several benchmarks (Zhang et al., 2025b; Fu et al., 2024b; Ma et al., 2024; Yang et al., 2025) have been proposed to evaluate spatial reasoning abilities, and existing methods (Chen et al., 2024a; Cheng et al., 2024; Hong et al., 2023; Driess et al., 2023; Chen et al., 2024e; Zhu et al., 2024a) typically enhance performance by increasing training data or incorporating additional structural inputs, such as depth, point clouds, or scene graphs. However, these structural inputs are often used without explicit modeling of spatial consistency, and structure-aware visual representations remain underexplored. In addition, while recent works have achieved unified 2D understanding and generation (Sun et al., 2023; 2024; Ye et al., 2024; Dong et al., 2024; Wu et al., 2024; Team, 2024; Wang et al., 2024a; Liu et al., 2024a; Wu et al., 2025; Chen et al., 2025; Huang et al., 2025), there is limited research on applying this concept to the spatial level. In contrast, we propose the first unified spatial framework, which not only handles spatial reasoning tasks but also generates 3D scenes based on a reference image and a specified view transformation.

Semantic and geometric representation Vision encoders (Liang et al., 2024; Zhai et al., 2023; Cherti et al., 2023; Jia et al., 2021; Li et al., 2021; 2022; 2023; Zhu et al., 2024b) trained with language supervision have demonstrated strong capabilities in semantic understanding, particularly in tasks involving open-vocabulary recognition and image-text alignment. However, these models typically lack spatial awareness and fail to capture geometric consistency across views. In contrast, geometric methods (Wang et al., 2024b; Leroy et al., 2024; Wang et al., 2025b) based on multi-view consistency learning focus on spatial correspondence and 3D reconstruction, but typically lack semantic understanding and are difficult to generalize to language-guided tasks. Other works (Ranzinger et al., 2024b;a; 2025; Heinrich et al., 2025; Sarıyıldız et al., 2025) explore multi-teacher feature distillation to combine semantic and geometric knowledge, but their training objectives focus on general-purpose representation fusion rather than geometric awareness.In contrast, we aim to pretrain the vision encoder with both semantic and geometric awareness, tailored for spatial unification.

3 Methodology

3.1 Pipeline Overview

Fig. 2 presents the overall workflow, with the training pipeline on the left and the inference process on the right. During training, *UniUGG* adopts a three-stage training strategy. First, as shown in Fig. 2 (a), we pretrain the vision encoder to learn geometric-semantic visual representations in stage 1, detailed in Sec. 3.2. Next, as illustrated in Fig. 2 (b), we pretrain the Spatial-VAE in stage 2, which compresses geometric-semantic information into a compact latent space. This module enhances efficient generation and facilitates producing sharper 3D point clouds, as discussed in Sec. 3.3. Finally, we perform unified training for spatial understanding and 3D generation in stage 3, while keeping both the ViT and the VAE encoder frozen, as depicted in Fig. 2 (c). The unified training procedure is elaborated in Sec. 3.3. During inference, *UniUGG* takes images, questions, or view-transformation as input and generates text answers and point clouds, as shown in Fig. 2 (d).

3.2 Vision encoder pretraining

In this section, we introduce our geometric-semantic learning strategy for vision encoder pretraining, shown in Fig. 3.

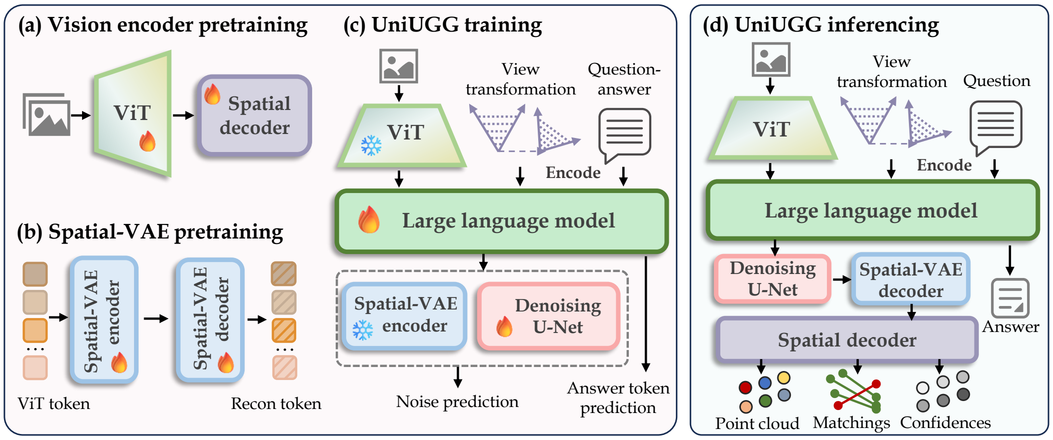

Figure 2: **Pipeline overview of *UniUGG*.** The left illustrates the three-stage training process, and the right shows the inference pipeline for spatial reasoning and 3D generation.

Encoder architecture Following the design of RADIOv2.5 (Heinrich et al., 2025), we adopt ViT-L/16 (Dosovitskiy et al., 2020) as our basic vision encoder to match the architecture of teachers, which allows us to benefit from its pretraining. Given an input image $\mathcal{I} \in \mathbb{R}^{H\times W\times 3}$, the vision encoder first partitions it into fixed-sized patches of size $p \times p$ pixels, then embeds them into hidden features of dimension d with learnable positional embeddings. After a series of Transformer blocks, the model finally produces a set $Z \in \mathcal{Z}$ of visual representations, where $\mathcal{Z} \in \mathbb{R}^{N\times d}$.

Multi-view geometric learning To enhance our encoder's spatial modeling, we adopt the MASt3R (Leroy et al., 2024) framework, retaining its decoder and spatial losses, while replacing the original encoder with ours. As shown in Fig. 3, paired images $\mathcal{I}^i, \mathcal{I}^j$ are encoded by our shared-weight encoder, producing two representations $\mathcal{Z}^i$ and $\mathcal{Z}^j$. A two-layer visual projector $f_\pi(\cdot)$ with GeLU activation processes each representation independently. Next, the projected features are fed into dual cross-attention decoders, yielding $\mathcal{H}^i, \mathcal{H}^j = \text{Decoder}(f_\pi(\mathcal{Z}^i), f_\pi(\mathcal{Z}^j))$. Finally, pointmaps $\text{X}_i^i, \text{X}_i^j \in \mathbb{R}^{H\times W\times 3}$ and confidence maps C^i, C^j are regressed from $[\mathcal{H}^i, \mathcal{H}^j]$, along with dense matching descriptors $\text{D}^i, \text{D}^j \in \mathbb{R}^{H\times W\times d_f}$, via a spatial head.

To extend our encoder for color-awareness, we implement an RGB head to reconstruct color information from encoded representation $\mathcal{Z}$, constrained by a composite loss:

$$\mathcal{L}_{rgb} = \lambda_{L_1}\cdot\|\hat{\mathcal{I}}-\mathcal{I}\|_{L_1} + \lambda_{\text{LP}}\cdot\text{LPIPS}(\hat{\mathcal{I}},\mathcal{I}), \quad (1)$$

where $\|\cdot\|_{L_1}$ denotes the *L1*-norm, and LPIPS (Zhang et al., 2018) captures perceptual similarity based on deep networks. The final training loss in the spatial branch is defined as:

$$\mathcal{L}_s = \mathcal{L}_{\text{conf}} + \lambda_1\mathcal{L}_{\text{match}} + \lambda_2\mathcal{L}_{\text{rgb}}, \quad (2)$$

where $\mathcal{L}_{\text{conf}}$ and $\mathcal{L}_{\text{match}}$ are confidence-aware regression loss and matching loss, respectively, defined in MASt3R.

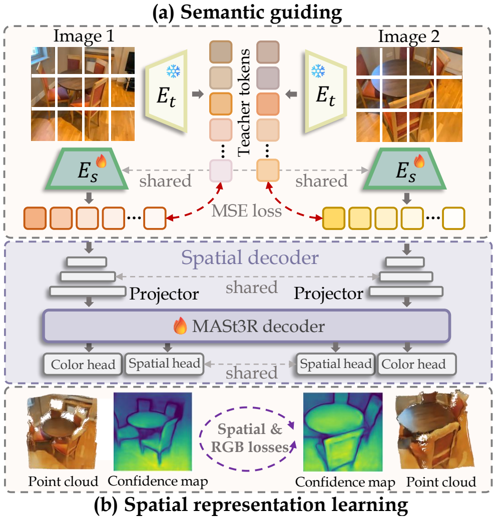

Figure 3: **Overview of our encoder pretraining pipeline.** (a) During semantic guiding, our student encoder learns to mimic the teacher's visual representations. (b) In spatial representation learning, the spatial decoder jointly refines predictions using information from both views.

Note that in the following, the visual projector, the MASt3R decoder, and the prediction heads are collectively referred to as the spatial decoder, as illustrated in Fig. 3.

Semantic knowledge guiding To enhance semantic understanding, we use the pretrained RADIOv2.5 as a teacher to guide our encoder. Given an input image, semantic tokens $\hat{\mathcal{Z}} \in \mathbb{R}^{N\times d}$ are extracted

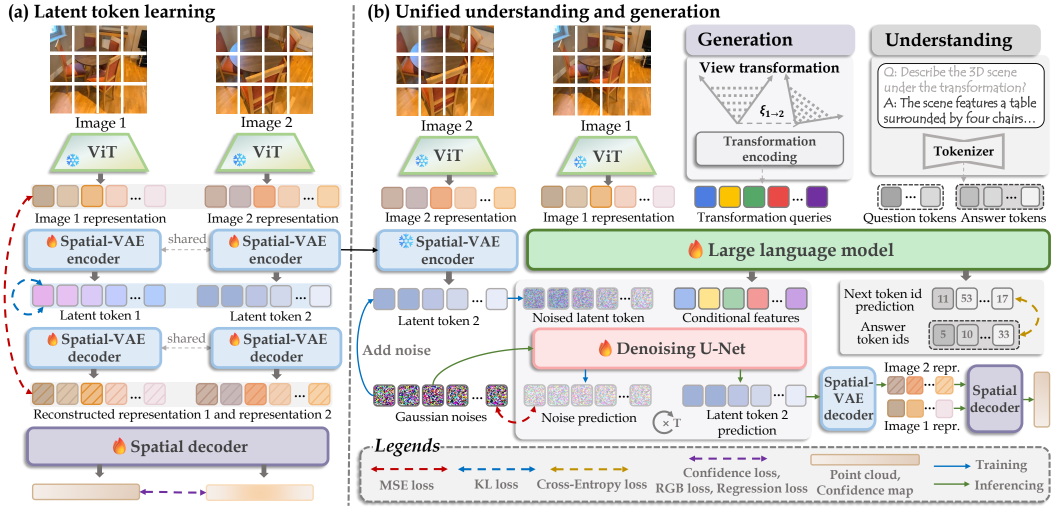

Figure 4: **Overview of *UniUGG* training.** (a) In the latent token learning stage (stage 2), visual representation is compressed using the Spatial-VAE, while the spatial decoder is linked for fine-tuning. (b) In the unified learning stage (stage 3), the reference image's visual representation and view transformation are input to an LLM, which outputs conditional features for noise prediction on latent token. The LLM also performs VQA-related training to maintain its understanding capability. During inferencing, *UniUGG* generates the visual representation of the target view, which, together with the reference representation, is decoded into the 3D scene.

from the teacher and aligned with student tokens $\mathcal{Z}$ via a weighted sum of cosine distance and smooth L_1 losses. To improve robustness, the loss is computed over a randomly sampled subset $\mathcal{C}$ of tokens. The guiding loss is defined as:

$$\mathcal{L}_{\text{KD}} = \alpha(1 - \frac{1}{n}\sum_{i\in\mathcal{C}} \cos(z_i, \hat{z}_i)) + \beta\frac{1}{n}\sum_{i\in\mathcal{C}} \|z_i - \hat{z}_i\|_{L_1}, \tag{3}$$

where $n = |\mathcal{C}|$ denotes the number of tokens. This alignment enforces consistency in both feature direction and magnitude.

3.3 Unified Understanding and Generation Learning

Leveraging prior knowledge, humans can imagine both geometric and semantic details of unobserved areas from a reference image. With this goal, we aim to enable LLMs to understand and reason scenes through spatial question answering, and imagine novel 3D structures under view changes.

Overall learning target Based on our encoder pretraining, we design *UniUGG* for unified spatial understanding and generation, detailed in Fig. 4 (b). For 3D generation, we leverage an LLM in combination with a diffusion model to generate the visual representation of the target view conditioned on a reference image and view transformation. The pretrained spatial decoder then processes the visual representations of both the reference image and the target view, decoding the 3D scene. For 3D understanding, we also perform supervised fine-tuning on the LLM at spatially grounded VQA tasks.

Latent token learning Directly generating high-dimensional representations is costly and unstable. To address this, we design and pretrain the Spatial-VAE with an encoder-decoder architecture to compress visual representations into a compact latent space, enabling efficient generation, shown in Fig. 4 (a). Given an image pair $\mathcal{I}^i, \mathcal{I}^j$, our pretrained vision encoder extracts visual representations $\mathcal{Z}^i, \mathcal{Z}^j \in \mathbb{R}^{N_h \times N_w \times d}$, which are encoded into 4-dimensional latent tokens $\mathcal{T}^i, \mathcal{T}^j \in \mathbb{R}^{L_h \times L_w \times 4}$ and then reconstructed back to $\bar{\mathcal{Z}}^i, \bar{\mathcal{Z}}^j$.

The Spatial-VAE optimization is guided by three loss terms: **(i)** Reconstruction loss $\mathcal{L}_{\text{mse}} = \left\|\bar{\mathcal{Z}}^i - \mathcal{Z}^i\right\|^2$. **(ii)** KL loss $\mathcal{L}_{\text{KL}} = D_{\text{KL}}(q(\mathcal{T}^i \,|\, \mathcal{Z}^i) \parallel p(\mathcal{T}^i)) + D_{\text{KL}}(q(\mathcal{T}^j \,|\, \mathcal{Z}^j) \parallel p(\mathcal{T}^j))$, where D_{KL} denotes the Kullback-Leibler divergence for latent distribution regularization. **(iii)** Spatial loss $\mathcal{L}_{\text{s}}$, defined in Eq. 2. Due to discrepancies between reconstructed and original representations, the pretrained spatial decoder may struggle to deal with the reconstructed representation. To address this and further guide compression, we feed the reconstructed representations into the spatial decoder and fine-tune it jointly with the Spatial-VAE in an end-to-end manner. The overall latent token learning loss $\mathcal{L}_{\text{vae}} = \mathcal{L}_{\text{s}} + \mathcal{L}_{\text{mse}} + \gamma \mathcal{L}_{\text{KL}}$, where γ is the weight for the KL loss term.

Spatial generation learning As shown in Fig. 4 (b), with the pretrained Spatial-VAE, the 3D generation can be modeled as generating the latent token conditioned on a reference image and a view transformation. This latent token is then decoded into the visual representation of the target-view using the VAE decoder. Subsequently, the 3D scene is decoded by the fine-tuned spatial decoder to the visual representations from both the reference and target views. Therefore, spatial generation learning is naturally the process of conditional noise prediction on the noisy latent token.

During training, the relative view transformation between $\mathcal{I}^i$ and $\mathcal{I}^j$ is encoded as a Plücker raymap (Plucker, 1865), represented as $\mathbf{P} \in \mathbb{R}^{N_h \times N_w \times 6}$. This raymap is then transformed into queries $\mathbf{q}$ using an MLP, so that suitable for processing by LLM. Subsequently, we feed the visual representation of $\mathcal{I}^i$, $\mathcal{Z}^i$, along with the transformation queries $\mathbf{q}$, into the LLM, which generates the conditional features $\mathbf{C}$.

The next step involves training the model to predict the noise in the noisy latent tokens. We encode $\mathcal{I}^j$'s visual representation $\mathcal{Z}^j$ into the latent token $\mathcal{T}^j$ via the pretrained VAE encoder. Gaussian noise is progressively added to the latent token $\mathcal{T}^j$ over several timesteps, creating a noisy latent token $\tilde{\mathcal{T}}_t^j$ for each timestep t. Specifically, the noise is added according to a schedule that increases with each timestep. The noisy latent token at each timestep is then passed through the denoising diffusion model along with the corresponding conditional features $\mathbf{C}$. At each timestep t, the model learns to predict the noise $\epsilon_\theta(\tilde{\mathcal{T}}_t^j|\mathbf{C}, t)$ added to the noisy latent token. The training target is minimizing the discrepancy between the predicted noise ϵ_θ and the ground-truth noise ϵ:

$$\mathcal{L}_{\text{gen}} = \mathbb{E}_{\mathcal{T}^j, \epsilon \sim \mathcal{N}(0,1), t} \left[\left\| \epsilon_\theta(\tilde{\mathcal{T}}_t^j|\mathbf{C}, t) - \epsilon \right\|^2 \right]. \tag{4}$$

At inference, we start from a noisy latent token $\tilde{\mathcal{T}}_T \sim \mathcal{N}(0,1)$ and iteratively denoise it using the reverse diffusion process. At each timestep t, the model predicts the noise to be removed, updating the latent token by $\tilde{\mathcal{T}}_{t-1} = \tilde{\mathcal{T}}_t - \epsilon_\theta(\tilde{\mathcal{T}}_t|\mathbf{C}, t)$. Here, $\mathbf{C}$ represents the conditional feature generated by the LLM, which takes the reference visual representation $\mathcal{Z}_r$ and an arbitrary view transformation as input. After T steps, the final latent token $\tilde{\mathcal{T}}_0$ is decoded into target view's visual representation $\mathcal{Z}_v$ by the Spatial-VAE decoder, and the full 3D structure is then decoded by the fine-tuned spatial decoder using both $\mathcal{Z}_r$ and $\mathcal{Z}_v$.

Spatial understanding learning Given an input image $\mathcal{I}$ and a question $\mathcal{Q}$, the model predicts an answer sequence $\mathbf{a} = \{\mathrm{a}_0, \mathrm{a}_1, ..., \mathrm{a}_N\}$ in an autoregressive manner. Firstly, the question $\mathcal{Q}$ is tokenized into language embeddings $\mathbf{q} = \{\mathrm{q}_0, \mathrm{q}_1, ..., \mathrm{q}_m\}$. Together with the image representation $\mathcal{Z}$, we feed these language tokens into the LLM. At step t, the LLM produces a distribution over the next token conditioned on ground-truth prefix $a_{<t}$. ***UniUGG*** is trained with teacher forcing using a token-level cross-entropy loss $\mathcal{L}_{\text{vqa}} = -\sum_{t=1}^{N} \log p_\theta(a_t|\mathcal{Z}, \mathbf{q}, a_{<t})$. Here, a_t is the ground-truth token at t. At inference, the prefix $a_{<t}$ is replaced by the previously generated tokens $\hat{a}_{<t}$.

4 Experiments

4.1 Implementation details

Vision encoder pretraining We initialize our vision encoder with RADIOv2.5-L (Heinrich et al., 2025), a ViT-Large model with 24 Transformer layers and a hidden size of 1024. The encoder is followed by a ViT-Base decoder initialized from MASt3R (Leroy et al., 2024). We pretrained our encoder on a mixture of ARKitScenes (Baruch et al., 2021) and ScanNet++(Yeshwanth et al., 2023) to capture geometric capabilities, and LAION-400M(Schuhmann et al., 2021) to capture semantic diversity. More training details can be found in Appendix A.2.

Training *UniUGG* The Spatial-VAE is trained on 2M co-viewing pairs from ARKitScenes and ScanNet++, with the KL loss weight $\gamma = 0.0001$. The detailed Spatial-VAE architecture can be found in Appendix A.2. For unified training in stage 3, the vision encoder and the Spatial-VAE are frozen, with only the LLM, projector, and diffusion model optimized. The training process follows three steps: **(i)** Projector is trained on LCS-558K (Liu et al., 2023) to align patch-level features with the LLM embedding space; **(ii)** LLM, diffusion model, and projector are jointly optimized on 2.4M spatial instruction-following samples from ShareGPT4V (Chen et al., 2024d) and ALLaVA (Chen et al., 2024b), along with 2M co-viewing pairs from ARKitScenes and ScanNet++; **(iii)** Model is further finetuned on SPAR (Zhang et al., 2025a), EMOVA (Chen et al., 2024c), and an additional 2M spatial sample pairs to enhance generalization in spatial QA and 3D generation tasks.

We use Qwen2.5-3B-Instruct (Bai et al., 2023) as the LLM backbone and stable-diffusion-v1-5 (Rombach et al., 2022) as the diffusion model. The AdamW optimizer with cosine learning rate decay and a warm-up ratio of 0.03 is used. The learning rate is set to 1×10^{-3} for step (i) and 2×10^{-5} for steps (ii) and (iii) in unified training. The global batch size is set to 256. Additional 0.25M samples are used for generation comparison, separate from the training data.

Training cost and computational resources Our pipeline adopts a three-stage training strategy as illustrated in Fig. 2. In stage 1, we pretrain the geometric-semantic encoder for 25 hours using 8× NVIDIA A6000 GPUs. In stage 2, the Spatial-VAE module is pretrained for 12 hours on the same 8× A6000 GPUs. In stage 3, we train the full *UniUGG* model on both spatial understanding and 3D generation tasks for about 46 hours on a cluster with 8 nodes, each equipped with 8 Ascend NPUs. During inference, we run our model on a single NVIDIA A6000 GPU. For spatial reasoning, given 16 input images at a resolution of 224×224, *UniUGG* achieves an inference latency of 350ms, utilizing bf16 precision and FlashAttention for acceleration. For 3D generation, *UniUGG* takes approximately 1.2s to generate a point cloud from a single reference image.

	Casual									**MipNeRF360**								
	Geometry			**Texture**			**All**			**Geometry**			**Texture**			**All**		
Feature	PSNR↑	SSIM↑	LPIPS↓	PSNR↑	SSIM↑	LPIPS↓	PSNR↑	SSIM↑	LPIPS↓	PSNR↑	SSIM↑	LPIPS↓	PSNR↑	SSIM↑	LPIPS↓	PSNR↑	SSIM↑	LPIPS↓
DINOv2	19.42	.6524	.3698	17.64	.5701	.3754	19.21	.6535	.4023	20.81	.4946	.3953	19.05	.4495	.3821	20.75	.4924	**.4684**
CLIP	19.21	.6552	.3719	17.46	.5669	.3743	19.05	.6582	.4084	20.80	.4982	.3913	19.28	.4543	.3807	20.88	.4984	.4773
DUSt3R	19.29	.6562	.3580	17.54	.5693	.3750	19.19	.6556	.4050	20.82	.5008	.3795	19.10	.4489	.3816	21.02	.5048	.4752
VGGT	19.36	.6590	.3549	17.47	.5645	.3751	19.23	.6604	.4103	20.93	.5120	.3639	19.25	.4497	.3828	21.17	.5102	.4892
RADIO	19.54	.6545	.3465	17.52	.5666	.3748	18.67	.6533	.4216	20.87	.5100	.3620	19.35	.4550	.3819	20.91	.5067	.5127
MASt3R	19.30	.6550	.3576	17.59	.5708	.3722	**19.37**	.6588	.4027	20.92	.5093	.3745	19.21	.4540	.3803	20.92	.5054	.4749
Ours	**19.80**	**.6643**	**.3449**	**17.81**	**.5850**	**.3559**	19.18	**.6693**	**.3955**	**21.28**	**.5337**	**.3562**	**19.72**	**.4848**	**.3595**	**21.31**	**.5264**	.4698

Table 1: **Results of novel view synthesis metrics on Feat2GS benchmark.** Our encoder outperforms others in most datasets across Geometry, Texture, and All probing modes. The best results are marked in **bold**, and the second best in underlined.

4.2 Evaluation of the geometric-semantic encoder

Evaluation on Feat2GS benchmark The Feat2GS benchmark (Chen et al., 2024g) evaluates novel view synthesis as a proxy task for assessing 3D awareness, which defines three evaluation modes: **(i)** Geometry: only geometry parameters are predicted from encoder features, while the texture is free-optimized for novel view rendering; **(ii)** Texture: only texture is predicted, with the geometry free-optimized; **(iii)** All: both geometry and texture are predicted from features. The encoders compared include DINOv2 (Oquab et al., 2023), CLIP (Radford et al., 2021), DUST3R encoder (Wang et al., 2024b), VGGT encoder (Wang et al., 2025a), AM-RADIO (Ranzinger et al., 2024b), and MASt3R encoder. As shown in Tab. 1, our vision encoder outperforms baselines in all three probing modes, achieving significant improvements. Detailed results are provided in Appendix A.3.1.

Evaluation on semantic perception and 3D vision tasks We comprehensively evaluate our pretrained vision encoder across a diverse set of tasks, including monocular and video depth estimation, image-level reasoning, and pixel-level visual understanding. Our method achieves highly competitive performance across all evaluations. Detailed results are provided in Appendix A.3.1.

Downstream task performance We assess the spatial understanding performance of our pretrained encoder by integrating it into a unified Vision-Language Model architecture based on Qwen2.5-3B-Instruct (Bai et al., 2023). We evaluate on a wide range of vision-language reasoning benchmarks. Spatial and geometric abilities are assessed through VSI-Bench (Yang et al., 2025), SPAR (Zhang et al., 2025a) and BLINK (Fu et al., 2024b), while general language understanding is tested on RealWorldQA (Miyanishi et al., 2021) and SEED-I (Li et al., 2024b). Compared models include both semantic-oriented encoders (CLIP-L/14, SigLIP-L/16 (Zhai et al., 2023), RADIOv2.5-L) and

Method	Para. (M)	VSI	BLINK	SPAR Low	SPAR Med.	SPAR High	Seed^{I}	Real World
Qwen2.5-ViT	669	35.56	37.81	36.50	36.67	39.89	41.81	44.97
CLIP-L/14	305	40.08	40.45	44.13	43.67	**52.33**	69.14	54.38
SigLIP-L/16	316	23.81	39.08	41.75	34.67	43.11	56.31	45.23
MASt3R Enc.	303	39.14	40.93	50.00	42.33	48.22	56.96	50.07
RADIOv2.5-L	320	39.75	42.92	50.44	47.95	52.13	**72.09**	57.38
UniUGG Enc.	320	**42.18**	**44.40**	**50.82**	**49.07**	51.89	71.65	**58.56**

Table 2: **Comparison of encoder performance on downstream vision-language reasoning benchmarks.** The VLM architecture is based on Qwen2.5-3B-Instruct, and all encoders are trained under the same settings to ensure fairness.

geometry-aware design (MASt3R encoder). All encoders are initialized from pretrained checkpoints and fine-tuned with the LLM under the same settings for fair comparison.

As shown in Tab. 2, on VSI-Bench, BLINK, and SPAR, our encoder (*UniUGG* Enc.) demonstrates clear advantages on spatial reasoning tasks, which require spatial relational understanding and geometric abstraction. Moreover, our method also achieves competitive performance on general QA benchmarks like RealWorldQA and SEED-I, showing that spatial enhancement does not significantly impair semantic generalization. Compared to the geometry-focused MASt3R encoder, our encoder shows more consistent performance across modalities. In general, our encoder can bridge geometry and semantics in a unified representation, balancing spatial perception and high-level semantics.

4.3 Evaluation of spatial understanding

To evaluate *UniUGG*'s spatial reasoning ability, we assess it on representative benchmarks, i.e., VSI-Bench, BLINK, 3DSRBench (Ma et al., 2024), and SPAR. We use three open-source LMMs—LLaVA (Liu et al., 2024b), InternVL2.5 (Chen et al., 2024h), Qwen2.5VL (Bai et al., 2025)—and one proprietary LMM, GPT-4o (Achiam et al., 2023), along with the state-of-the-art 2D unified framework Janus-Pro (Chen et al., 2025) for comparison. Results shown in Tab. 3, our *UniUGG* achieves superior performance across most benchmarks. In particular, on VSI-Bench, our model outperforms the second-best one by 17.9%. It demonstrates that *UniUGG* can capture fine-grained spatial relations by jointly modeling 3D structure and visual-language reasoning. Additional evaluations on SQA3D (Ma et al., 2022), ScanQA (Azuma et al., 2022), and ScanRefer (Chen et al., 2020) are provided in Appendix A.3.2. It should be noted that *UniUGG* is designed for multi-view spatial understanding, where the model learns geometry from 2D inputs. Therefore, on these 3D benchmarks, our model still shows a performance gap compared to 3D-enhanced methods.

4.4 Evaluation of 3D generation

Quantitative generation comparison and ablations We compare *UniUGG* with baselines and perform ablation studies to evaluate the quality of the generated outputs. Given a reference image and a view transformation, the setup generates the corresponding spatial structure for the novel view. The generated point cloud is then projected back onto the image plane, producing a colored 2D image. These generated images are compared to the real images (Ground truth) using the Fréchet inception distance (FID), kernel inception distance (KID), and LPIPS. Quantitative and qualitative results are presented in Tab. 3 and Fig. 5, respectively.

The encoder from our pretraining strategy (ID g) significantly improves generation quality, outperforming both the RADIOv2.5-L (ID a) and MASt3R encoder (ID b). This shows that simply incorporating geometric or semantic information is insufficient, and fusing both is more effective in a unified framework. From the *UniUGG* settings, we observe a notable performance drop when the spatial decoder is not fine-tuned during VAE training (ID c). Additionally, omitting the Spatial-VAE and diffusion models (ID d), and having the LLM directly predict the target-view representation, results in suboptimal performance. By the way, removing the Spatial-VAE only and training generation directly on the original representation also fails to generate valid results. These results demonstrate the Spatial-VAE and related training paradigms are the key to successful 3D generation. Finally, we compare *UniUGG* with baselines, CUT3R (Wang et al., 2025b) and LVSM (Jin et al., 2025). While CUT3R (ID e) predicts 3D structures from pre-observed data and raymap, and LVSM (ID f) generates

Method	VSI	BLINK	3DSR	SPAR			
				Low	Med.	High	Avg.
LLaVA-v1.5-7B	18.0	37.1	38.1	10.9	26.5	34.1	23.7
LLaVA-NeXT-7B	20.6	41.8	48.4	8.5	4.8	20.2	13.2
InternVL2.5-8B	32.5	54.8	50.9	29.5	31.9	43.8	36.3
Qwen2.5-VL-7B	30.3	56.4	48.4	28.8	23.0	40.3	33.1
GPT-4o	34.0	**60.0**	44.2	36.9	26.5	43.8	38.1
∗Janus-Pro-1B	-	38.9	50.0	10.7	24.7	30.8	20.6
∗Janus-Pro-7B	-	40.5	**53.7**	27.3	24.6	33.9	28.6
UniUGG-3B (Ours)	**40.1**	43.6	52.1	**50.8**	**41.7**	**45.7**	**47.2**

ID Method	ARKitScenes			ScanNet++		
	FID↓	KID↓	LPIPS↓	FID↓	KID↓	LPIPS↓
(a) w/ RADIO	64.16	.0518	.4904	73.69	.0614	.4629
(b) w/ MASt3R Enc.	81.18	.0691	.5076	86.79	.0803	.5242
(c) w/o Dec. finetune	149.97	.1447	.5301	168.05	.1686	.4945
(d) w/o Diffusion	87.51	.0672	**.4494**	114.93	.0955	.4345
(e) CUT3R	138.54	.1128	.5758	130.76	.1051	.5637
(f) LVSM	269.45	.3088	.5067	414.63	.5117	.5865
(g) *UniUGG* (Ours)	**55.01**	**.0425**	.4849	**55.64**	**.0442**	**.4263**

Table 3: **Comparison of 3D understanding and generation performance.** *Left*: 3D understanding performance on various spatial reasoning benchmarks. ∗denotes 2D understanding and generation method. *Right*: Quantitative spatial generation comparison on ARKitScenes and ScanNet++ datasets. ID(a) to ID(d) represent the ablation of our model.

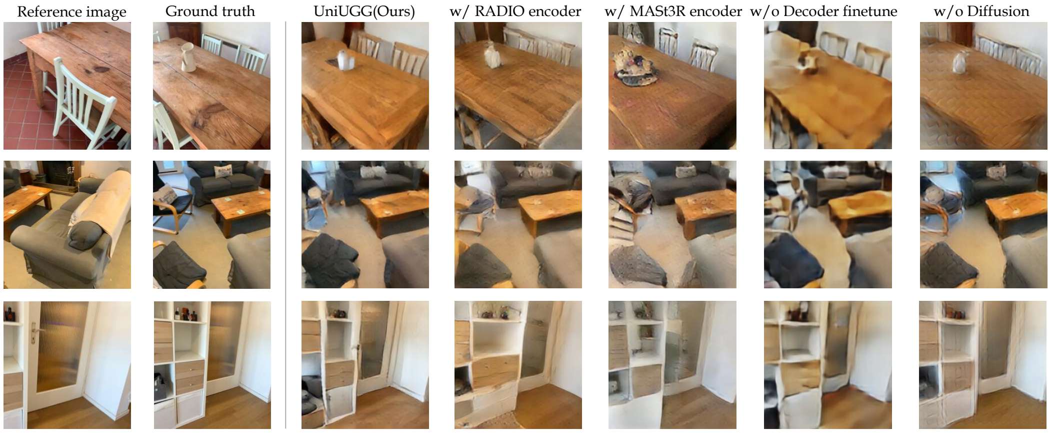

Figure 5: **Qualitative ablation on 2D projected views from 3D generation.** Our *UniUGG*, including the geometric-semantic encoder, Spatial-VAE, and associated training paradigm, leads to noticeably better generation results, in terms of geometric accuracy and color consistency.

target-view 2D images, both fall short in performance due to their lack of imaginative capabilities. This highlights the superiority of our method in 3D generation.

Qualitative understanding and generation comparison We further qualitatively assess our *UniUGG* with CUT3R, shown in Fig. 6. From the perspective of the generated area, *UniUGG* accurately identifies which parts of the geometric structure need to be generated. Additionally, in terms of texture and semantic details, *UniUGG* effectively leverages the reference image to plausibly infer new structures, such as windows and chairs. We also demonstrate the understanding capabilities of *UniUGG* by generating captions for the scene from the generated visual representations. *UniUGG* can provide accurate descriptions of the 3D structure, even for parts that were previously unseen. In contrast, the baseline struggles to complete missing regions and lacks coherence in structural details, let alone understanding the scene. These results highlight the strengths of *UniUGG* in unified spatial understanding and 3D generation. We provide additional visualizations—including feature matching, evaluation under extreme view transformations, and failure cases—in Appendix A.3.3

5 Conclusion and Limitations

In this paper, we introduce *UniUGG*, the first unified framework for spatial generation and understanding, capable of spatial-level VQA and generating 3D scenes. We propose a geometric-semantic learning strategy to pretrain the vision encoder, enhancing its spatial modeling capabilities. This significantly improves both the generation and understanding aspects of our unified framework and yields strong performance on downstream tasks. Moreover, we design the Spatial-VAE for achieving efficient 3D generation, and link the spatial decoder for fine-tuning to ensure sharper 3D scene decoding. Extensive evaluations showcasing *UniUGG*'s ability to handle both 3D generation and

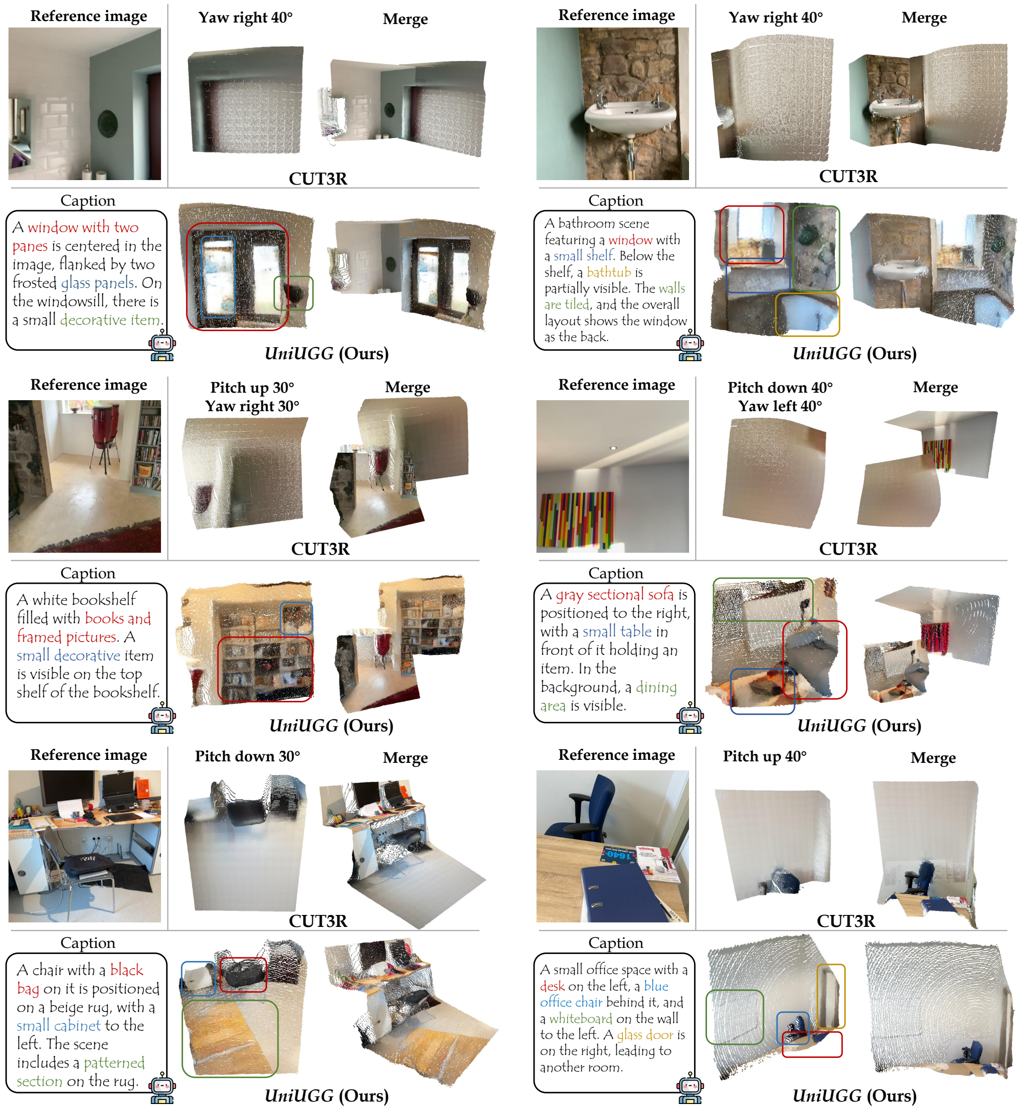

A window with two panes is centered in the image, flanked by two frosted glass panels. On the windowsill, there is a small decorative item.

A bathroom scene featuring a window with a small shelf. Below the shelf, a bathtub is partially visible. The walls are tiled, and the overall layout shows the window as the back.

A white bookshelf filled with books and framed pictures. A small decorative item is visible on the top shelf of the bookshelf.

A gray sectional sofa is positioned to the right, with a small table in front of it holding an item. In the background, a dining area is visible.

A chair with a black bag on it is positioned on a beige rug, with a small cabinet to the left. The scene includes a patterned section on the rug.

A small office space with a desk on the left, a blue office chair behind it, and a whiteboard on the wall to the left. A glass door is on the right, leading to another room.

Figure 6: **Qualitative 3D generation comparison.** *UniUGG* accurately captures the input view transformation and leverages the reference image to 'imagine' fine-grained spatial structures, and outputs correct captioning. In contrast, the baseline method only produces coarse and fuzzy geometry.

spatial VQA tasks effectively. However, further enhancing 3D generation capabilities in unified models remains a key challenge for future research. Our framework still has several limitations, including the lack of controllable generation driven by language and the inability to perform freeform editing of the generated content. As a preliminary exploration toward unified 3D modeling, our method does not yet support interactive multi-round scene generation and editing, which also needs to be solved in the future.

References

Josh Achiam, Steven Adler, Sandhini Agarwal, Lama Ahmad, Ilge Akkaya, Florencia Leoni Aleman, Diogo Almeida, Janko Altenschmidt, Sam Altman, Shyamal Anadkat, et al. Gpt-4 technical report. *arXiv preprint*, 2023.

Jean-Baptiste Alayrac, Jeff Donahue, Pauline Luc, Antoine Miech, Iain Barr, Yana Hasson, Karel Lenc, Arthur Mensch, Katherine Millican, Malcolm Reynolds, et al. Flamingo: a visual language model for few-shot learning. *NeurIPS*, 2022.

Daichi Azuma, Taiki Miyanishi, Shuhei Kurita, and Motoaki Kawanabe. Scanqa: 3d question answering for spatial scene understanding. In *CVPR*, 2022.

Jinze Bai, Shuai Bai, Yunfei Chu, Zeyu Cui, Kai Dang, Xiaodong Deng, Yang Fan, Wenbin Ge, Yu Han, Fei Huang, et al. Qwen technical report. *arXiv preprint*, 2023.

Shuai Bai, Keqin Chen, Xuejing Liu, Jialin Wang, Wenbin Ge, Sibo Song, Kai Dang, Peng Wang, Shijie Wang, Jun Tang, et al. Qwen2. 5-vl technical report. *arXiv preprint*, 2025.

Gilad Baruch, Zhuoyuan Chen, Afshin Dehghan, Tal Dimry, Yuri Feigin, Peter Fu, Thomas Gebauer, Brandon Joffe, Daniel Kurz, Arik Schwartz, and Elad Shulman. ARKitscenes - a diverse real-world dataset for 3d indoor scene understanding using mobile RGB-d data. In *NeurIPS Datasets and Benchmarks Track (Round 1)*, 2021.

Boyuan Chen, Zhuo Xu, Sean Kirmani, Brain Ichter, Dorsa Sadigh, Leonidas Guibas, and Fei Xia. Spatialvlm: Endowing vision-language models with spatial reasoning capabilities. In *CVPR*, 2024a.

Dave Zhenyu Chen, Angel X Chang, and Matthias Nießner. Scanrefer: 3d object localization in rgb-d scans using natural language. In *ECCV*, 2020.

Guiming Hardy Chen, Shunian Chen, Ruifei Zhang, Junying Chen, Xiangbo Wu, Zhiyi Zhang, Zhihong Chen, Jianquan Li, Xiang Wan, and Benyou Wang. Allava: Harnessing gpt4v-synthesized data for lite vision-language models. *arXiv preprint*, 2024b.

Kai Chen, Yunhao Gou, Runhui Huang, Zhili Liu, Daxin Tan, Jing Xu, Chunwei Wang, Yi Zhu, Yihan Zeng, Kuo Yang, et al. Emova: Empowering language models to see, hear and speak with vivid emotions. *arXiv preprint*, 2024c.

Lin Chen, Jinsong Li, Xiaoyi Dong, Pan Zhang, Conghui He, Jiaqi Wang, Feng Zhao, and Dahua Lin. Sharegpt4v: Improving large multi-modal models with better captions. In *ECCV*, 2024d.

Shizhe Chen, Pierre-Louis Guhur, Makarand Tapaswi, Cordelia Schmid, and Ivan Laptev. Language conditioned spatial relation reasoning for 3d object grounding. *NeurIPS*, 2022.

Sijin Chen, Xin Chen, Chi Zhang, Mingsheng Li, Gang Yu, Hao Fei, Hongyuan Zhu, Jiayuan Fan, and Tao Chen. Ll3da: Visual interactive instruction tuning for omni-3d understanding reasoning and planning. In *CVPR*, 2024e.

Xiaokang Chen, Zhiyu Wu, Xingchao Liu, Zizheng Pan, Wen Liu, Zhenda Xie, Xingkai Yu, and Chong Ruan. Janus-pro: Unified multimodal understanding and generation with data and model scaling. *arXiv preprint*, 2025.

Yilun Chen, Shuai Yang, Haifeng Huang, Tai Wang, Runsen Xu, Ruiyuan Lyu, Dahua Lin, and Jiangmiao Pang. Grounded 3d-llm with referent tokens. *arXiv preprint*, 2024f.

Yue Chen, Xingyu Chen, Anpei Chen, Gerard Pons-Moll, and Yuliang Xiu. Feat2gs: Probing visual foundation models with gaussian splatting. *arXiv preprint*, 2024g.

Zhe Chen, Weiyun Wang, Yue Cao, Yangzhou Liu, Zhangwei Gao, Erfei Cui, Jinguo Zhu, Shenglong Ye, Hao Tian, Zhaoyang Liu, et al. Expanding performance boundaries of open-source multimodal models with model, data, and test-time scaling. *arXiv preprint*, 2024h.

An-Chieh Cheng, Hongxu Yin, Yang Fu, Qiushan Guo, Ruihan Yang, Jan Kautz, Xiaolong Wang, and Sifei Liu. Spatialrgpt: Grounded spatial reasoning in vision language models. *arXiv preprint*, 2024.

Mehdi Cherti, Romain Beaumont, Ross Wightman, Mitchell Wortsman, Gabriel Ilharco, Cade Gordon, Christoph Schuhmann, Ludwig Schmidt, and Jenia Jitsev. Reproducible scaling laws for contrastive language-image learning. In *CVPR*, 2023.

MMSegmentation Contributors. Mmsegmentation: Openmmlab semantic segmentation toolbox and benchmark, 2020.

Timothée Darcet, Maxime Oquab, Julien Mairal, and Piotr Bojanowski. Vision transformers need registers. *arXiv preprint*, 2023.

Jia Deng, Wei Dong, Richard Socher, Li-Jia Li, Kai Li, and Li Fei-Fei. Imagenet: A large-scale hierarchical image database. In *CVPR*, 2009.

Runpei Dong, Chunrui Han, Yuang Peng, Zekun Qi, Zheng Ge, Jinrong Yang, Liang Zhao, Jianjian Sun, Hongyu Zhou, Haoran Wei, Xiangwen Kong, Xiangyu Zhang, Kaisheng Ma, and Li Yi. DreamLLM: Synergistic multimodal comprehension and creation. In *ICLR*, 2024.

Alexey Dosovitskiy, Lucas Beyer, Alexander Kolesnikov, Dirk Weissenborn, Xiaohua Zhai, Thomas Unterthiner, Mostafa Dehghani, Matthias Minderer, Georg Heigold, Sylvain Gelly, et al. An image is worth 16x16 words: Transformers for image recognition at scale. *arXiv preprint*, 2020.

Danny Driess, Fei Xia, Mehdi SM Sajjadi, Corey Lynch, Aakanksha Chowdhery, Ayzaan Wahid, Jonathan Tompson, Quan Vuong, Tianhe Yu, Wenlong Huang, et al. Palm-e: An embodied multimodal language model. 2023.

Mark Everingham, SM Ali Eslami, Luc Van Gool, Christopher KI Williams, John Winn, and Andrew Zisserman. The pascal visual object classes challenge: A retrospective. *IJCV*, 2015.

Rao Fu, Jingyu Liu, Xilun Chen, Yixin Nie, and Wenhan Xiong. Scene-llm: Extending language model for 3d visual understanding and reasoning. *arXiv preprint*, 2024a.

Xingyu Fu, Yushi Hu, Bangzheng Li, Yu Feng, Haoyu Wang, Xudong Lin, Dan Roth, Noah A Smith, Wei-Chiu Ma, and Ranjay Krishna. Blink: Multimodal large language models can see but not perceive. In *ECCV*, 2024b.

Greg Heinrich, Mike Ranzinger, Yin Hongxu, Yao Lu, Jan Kautz, Andrew Tao, Bryan Catanzaro, and Pavlo Molchanov. Radiov2. 5: Improved baselines for agglomerative vision foundation models. In *CVPR*, 2025.

Yining Hong, Haoyu Zhen, Peihao Chen, Shuhong Zheng, Yilun Du, Zhenfang Chen, and Chuang Gan. 3d-llm: Injecting the 3d world into large language models. *NeurIPS*, 2023.

Haifeng Huang, Yilun Chen, Zehan Wang, Rongjie Huang, Runsen Xu, Tai Wang, Luping Liu, Xize Cheng, Yang Zhao, Jiangmiao Pang, et al. Chat-scene: Bridging 3d scene and large language models with object identifiers. *arXiv preprint*, 2023a.

Jiangyong Huang, Silong Yong, Xiaojian Ma, Xiongkun Linghu, Puhao Li, Yan Wang, Qing Li, Song-Chun Zhu, Baoxiong Jia, and Siyuan Huang. An embodied generalist agent in 3d world. *arXiv preprint*, 2023b.

Runhui Huang, Chunwei Wang, Junwei Yang, Guansong Lu, Yunlong Yuan, Jianhua Han, Lu Hou, Wei Zhang, Lanqing Hong, Hengshuang Zhao, et al. Illume+: Illuminating unified mllm with dual visual tokenization and diffusion refinement. *arXiv preprint*, 2025.

Shijia Huang, Yilun Chen, Jiaya Jia, and Liwei Wang. Multi-view transformer for 3d visual grounding. In *CVPR*, 2022.

Chao Jia, Yinfei Yang, Ye Xia, Yi-Ting Chen, Zarana Parekh, Hieu Pham, Quoc Le, Yun-Hsuan Sung, Zhen Li, and Tom Duerig. Scaling up visual and vision-language representation learning with noisy text supervision. In *ICML*, 2021.

Haian Jin, Hanwen Jiang, Hao Tan, Kai Zhang, Sai Bi, Tianyuan Zhang, Fujun Luan, Noah Snavely, and Zexiang Xu. Lvsm: A large view synthesis model with minimal 3d inductive bias. In *ICLR*, 2025.

Alexander Kirillov, Eric Mintun, Nikhila Ravi, Hanzi Mao, Chloe Rolland, Laura Gustafson, Tete Xiao, Spencer Whitehead, Alexander C Berg, Wan-Yen Lo, et al. Segment anything. In *ICCV*, 2023.

Vincent Leroy, Yohann Cabon, and Jérôme Revaud. Grounding image matching in 3d with mast3r. In *ECCV*, 2024.

Bo Li, Yuanhan Zhang, Dong Guo, Renrui Zhang, Feng Li, Hao Zhang, Kaichen Zhang, Peiyuan Zhang, Yanwei Li, Ziwei Liu, et al. Llava-onevision: Easy visual task transfer. *arXiv preprint*, 2024a.

Bohao Li, Yuying Ge, Yixiao Ge, Guangzhi Wang, Rui Wang, Ruimao Zhang, and Ying Shan. Seed-bench: Benchmarking multimodal large language models. In *CVPR*, 2024b.

Junnan Li, Ramprasaath Selvaraju, Akhilesh Gotmare, Shafiq Joty, Caiming Xiong, and Steven Chu Hong Hoi. Align before fuse: Vision and language representation learning with momentum distillation. *NeurIPS*, 2021.

Junnan Li, Dongxu Li, Caiming Xiong, and Steven Hoi. Blip: Bootstrapping language-image pre-training for unified vision-language understanding and generation. In *ICML*, 2022.

Junnan Li, Dongxu Li, Silvio Savarese, and Steven Hoi. Blip-2: Bootstrapping language-image pre-training with frozen image encoders and large language models. In *ICML*, 2023.

Zijing Liang, Yanjie Xu, Yifan Hong, Penghui Shang, Qi Wang, Qiang Fu, and Ke Liu. A survey of multimodel large language models. In *CAICE*, 2024.

Hao Liu, Wilson Yan, Matei Zaharia, and Pieter Abbeel. World model on million-length video and language with blockwise ringattention. *arXiv preprint*, 2024a.

Haotian Liu, Chunyuan Li, Qingyang Wu, and Yong Jae Lee. Visual instruction tuning. *NeurIPS*, 2023.

Haotian Liu, Chunyuan Li, Yuheng Li, and Yong Jae Lee. Improved baselines with visual instruction tuning. In *CVPR*, 2024b.

Wufei Ma, Haoyu Chen, Guofeng Zhang, Celso M de Melo, Alan Yuille, and Jieneng Chen. 3dsrbench: A comprehensive 3d spatial reasoning benchmark. *arXiv preprint*, 2024.

Xiaojian Ma, Silong Yong, Zilong Zheng, Qing Li, Yitao Liang, Song-Chun Zhu, and Siyuan Huang. Sqa3d: Situated question answering in 3d scenes. *arXiv preprint*, 2022.

Taiki Miyanishi, Takuya Maekawa, and Motoaki Kawanabe. Sim2realqa: Using life simulation to solve question answering real-world events. *IEEE Access*, 2021.

Maxime Oquab, Timothée Darcet, Théo Moutakanni, Huy Vo, Marc Szafraniec, Vasil Khalidov, Pierre Fernandez, Daniel Haziza, Francisco Massa, Alaaeldin El-Nouby, et al. Dinov2: Learning robust visual features without supervision. *arXiv preprint*, 2023.

Julius Plucker. Xvii. on a new geometry of space. *Philosophical Transactions of the Royal Society of London*, 1865.

Alec Radford, Jong Wook Kim, Chris Hallacy, Aditya Ramesh, Gabriel Goh, Sandhini Agarwal, Girish Sastry, Amanda Askell, Pamela Mishkin, Jack Clark, et al. Learning transferable visual models from natural language supervision. In *ICML*, 2021.

Mike Ranzinger, Jon Barker, Greg Heinrich, Pavlo Molchanov, Bryan Catanzaro, and Andrew Tao. Phi-s: Distribution balancing for label-free multi-teacher distillation. *arXiv preprint*, 2024a.

Mike Ranzinger, Greg Heinrich, Jan Kautz, and Pavlo Molchanov. Am-radio: Agglomerative vision foundation model reduce all domains into one. In *CVPR*, 2024b.

Mike Ranzinger, Greg Heinrich, Pavlo Molchanov, Jan Kautz, Bryan Catanzaro, and Andrew Tao. Featsharp: Your vision model features, sharper. *arXiv preprint*, 2025.

Robin Rombach, Andreas Blattmann, Dominik Lorenz, Patrick Esser, and Björn Ommer. High-resolution image synthesis with latent diffusion models. In *CVPR*, 2022.

Mert Bülent Sarıyıldız, Philippe Weinzaepfel, Thomas Lucas, Pau de Jorge, Diane Larlus, and Yannis Kalantidis. Dune: Distilling a universal encoder from heterogeneous 2d and 3d teachers. In *CVPR*, 2025.

Christoph Schuhmann, Richard Vencu, Romain Beaumont, Robert Kaczmarczyk, Clayton Mullis, Aarush Katta, Theo Coombes, Jenia Jitsev, and Aran Komatsuzaki. Laion-400m: Open dataset of clip-filtered 400 million image-text pairs. *arXiv preprint*, 2021.

Nathan Silberman, Derek Hoiem, Pushmeet Kohli, and Rob Fergus. Indoor segmentation and support inference from rgbd images. In *ECCV*, 2012.

Quan Sun, Qiying Yu, Yufeng Cui, Fan Zhang, Xiaosong Zhang, Yueze Wang, Hongcheng Gao, Jingjing Liu, Tiejun Huang, and Xinlong Wang. Generative pretraining in multimodality. *arXiv preprint*, 2023.

Quan Sun, Yufeng Cui, Xiaosong Zhang, Fan Zhang, Qiying Yu, Zhengxiong Luo, Yueze Wang, Yongming Rao, Jingjing Liu, Tiejun Huang, and Xinlong Wang. Generative multimodal models are in-context learners. In *CVPR*, 2024.

Chameleon Team. Chameleon: Mixed-modal early-fusion foundation models. *arXiv preprint*, 2024.

Chunwei Wang, Guansong Lu, Junwei Yang, Runhui Huang, Jianhua Han, Lu Hou, Wei Zhang, and Hang Xu. Illume: Illuminating your llms to see, draw, and self-enhance. *arXiv preprint*, 2024a.

Hengyi Wang and Lourdes Agapito. 3d reconstruction with spatial memory. *arXiv preprint*, 2024.

Jianyuan Wang, Minghao Chen, Nikita Karaev, Andrea Vedaldi, Christian Rupprecht, and David Novotny. Vggt: Visual geometry grounded transformer. In *CVPR*, 2025a.

Qianqian Wang, Yifei Zhang, Aleksander Holynski, Alexei A Efros, and Angjoo Kanazawa. Continuous 3d perception model with persistent state. In *CVPR*, 2025b.

Shuzhe Wang, Vincent Leroy, Yohann Cabon, Boris Chidlovskii, and Jerome Revaud. Dust3r: Geometric 3d vision made easy. In *CVPR*, 2024b.

Chengyue Wu, Xiaokang Chen, Zhiyu Wu, Yiyang Ma, Xingchao Liu, Zizheng Pan, Wen Liu, Zhenda Xie, Xingkai Yu, Chong Ruan, et al. Janus: Decoupling visual encoding for unified multimodal understanding and generation. In *CVPR*, 2025.

Yecheng Wu, Zhuoyang Zhang, Junyu Chen, Haotian Tang, Dacheng Li, Yunhao Fang, Ligeng Zhu, Enze Xie, Hongxu Yin, Li Yi, et al. Vila-u: a unified foundation model integrating visual understanding and generation. *arXiv preprint*, 2024.

Jihan Yang, Shusheng Yang, Anjali W Gupta, Rilyn Han, Li Fei-Fei, and Saining Xie. Thinking in space: How multimodal large language models see, remember, and recall spaces. In *CVPR*, 2025.

Hanrong Ye, De-An Huang, Yao Lu, Zhiding Yu, Wei Ping, Andrew Tao, Jan Kautz, Song Han, Dan Xu, Pavlo Molchanov, et al. X-vila: Cross-modality alignment for large language model. *arXiv preprint*, 2024.

Chandan Yeshwanth, Yueh-Cheng Liu, Matthias Nießner, and Angela Dai. Scannet++: A high-fidelity dataset of 3d indoor scenes. In *ICCV*, 2023.

Xiaohua Zhai, Basil Mustafa, Alexander Kolesnikov, and Lucas Beyer. Sigmoid loss for language image pre-training. In *ICCV*, 2023.

Jiahui Zhang, Yurui Chen, Yanpeng Zhou, Yueming Xu, Ze Huang, Jilin Mei, Junhui Chen, Yu-Jie Yuan, Xinyue Cai, Guowei Huang, et al. From flatland to space: Teaching vision-language models to perceive and reason in 3d. *arXiv preprint*, 2025a.

Jiahui Zhang, Yurui Chen, Yanpeng Zhou, Yueming Xu, Ze Huang, Jilin Mei, Junhui Chen, Yujie Yuan, Xinyue Cai, Guowei Huang, Xingyue Quan, Hang Xu, and Li Zhang. From flatland to space: Teaching vision-language models to perceive and reason in 3d. *NeurIPS*, 2025b.

Junyi Zhang, Charles Herrmann, Junhwa Hur, Varun Jampani, Trevor Darrell, Forrester Cole, Deqing Sun, and Ming-Hsuan Yang. Monst3r: A simple approach for estimating geometry in the presence of motion. *arXiv preprint*, 2024.

Richard Zhang, Phillip Isola, Alexei A Efros, Eli Shechtman, and Oliver Wang. The unreasonable effectiveness of deep features as a perceptual metric. In *CVPR*, 2018.

Duo Zheng, Shijia Huang, and Liwei Wang. Video-3d llm: Learning position-aware video representation for 3d scene understanding. *arXiv preprint*, 2024.

Bolei Zhou, Hang Zhao, Xavier Puig, Tete Xiao, Sanja Fidler, Adela Barriuso, and Antonio Torralba. Semantic understanding of scenes through the ade20k dataset. *IJCV*, 2019.

Chenming Zhu, Tai Wang, Wenwei Zhang, Jiangmiao Pang, and Xihui Liu. Llava-3d: A simple yet effective pathway to empowering lmms with 3d-awareness. *arXiv preprint*, 2024a.

Yi Zhu, Zhou Yanpeng, Chunwei Wang, Yang Cao, Jianhua Han, Lu Hou, and Hang Xu. Unit: Unifying image and text recognition in one vision encoder. *NeurIPS*, 2024b.

A Appendix

In Appendix, we provide additional technical details and more detailed experimental validations in terms of our method, comparison, and visualization.

A.1 Use of Large Language Models

We used GPT-4o to polish the language and improve the clarity of our manuscript, such as improving grammar and phrasing. The model did not contribute to the core research content of the manuscript, including mathematical formulations, algorithms, and related results.

A.2 Additional implementation details

Vision encoder pretraining In the experiments, the patch size is set to 16×16, producing 768 tokens of dimension 1024. The training uses AdamW optimizer with cosine decay over 5 epochs, with loss weights $\lambda_{L_1} = 1.0$, $\lambda_{LP} = 0.5$,$\lambda_1 = 1.0$, $\lambda_2 = 1.0$, and semantic guiding loss weights $\alpha = 0.9$, $\beta = 0.1$.

Downstream task evaluation To assess the effectiveness of the pretrained encoder across downstream tasks, we adopt an experimental configuration in which the encoder, projector, and LLM are jointly trained in an end-to-end fashion. While this setting follows the stage 3 training pipeline as described in the *Sec. 4.1 'Training UniUGG' part of the main text*, it differs in two key aspects: the encoder is updated during training, and no additional co-viewing sample pairs are included. This design allows us to evaluate the performance of different encoders on both spatial understanding and general reasoning tasks fairly.

We assess the downstream performance of our pretrained encoder and other encoders by integrating them into a unified Vision-Language Model (VLM) architecture based on Qwen2.5-3B-Instruct (Bai et al., 2023). All models are trained with the same pipeline, jointly optimizing the encoder, visual projector, and LLM. This design ensures fair comparison under identical supervision and model capacity. All encoders are initialized from their respective pretrained checkpoints and jointly finetuned with the LLM under the same settings to ensure fair comparison.

Spatial-VAE architecture. The detailed Spatial-VAE architecture is provided in Tab. 4. The architecture follows an encoder-decoder design tailored for compressing and reconstructing visual representations. The encoder first reshapes the visual representation inputs into a 2D feature map, applies a series of convolutional and attention layers, and finally outputs the latent mean and variance for sampling. The decoder mirrors this process by reconstructing the visual representations from the sampled latent features using a combination of attention blocks and convolutional layers. Transformer-based attention modules are used in both the encoder and decoder to model long-range dependencies across spatial positions, enhancing semantic fidelity during compression and reconstruction.

Layer	Description	Output shape
Sptatial-VAE encoder		
0	Reshaped input	[b, 1024, 14, 14]
1	Initial convolution	[b, 256, 14, 14]
2	Upsample 1 (convtranspose)	[b, 128, 28, 28]
3	Upsample 2 (convolution)	[b, 128, 28, 28]
4	Transformer blocks	[b, 784, 128]
5	Flattened attention output	[b, 128, 28, 28]
6	μ convolution	[b, 4, 28, 28]
7	Log-variance convolution	[b, 4, 28, 28]
8	Reparameterization	[b, 4, 28, 28]
9	KL divergence loss	scalar (mean of log variance)
Sptatial-VAE decoder		
0	Input	[b, 4, 28, 28]
1	Pre-convolution	[b, 128, 28, 28]
2	Flattened attention output	[b, 784, 128]
3	Transformer blocks	[b, 784, 128]
4	Reshaped attention output	[b, 128, 28, 28]
5	Downsample 1 (convolution)	[b, 128, 28, 28]
6	Downsample 2 (convolution)	[b, 256, 14, 14]
7	Final convolution	[b, 1024, 14, 14]
8	Output reshaped	[b, 196, 1024]

Table 4: **Detailed Spatial-VAE architecture.** Our model follows an encoder-decoder design.

	LLFF									**DL3DV**									**Casual**								
	Geometry			Texture			All			Geometry			Texture			All			Geometry			Texture			All		
Feature	PSNR↑	SSIM↑	LPIPS↓	PSNR↑	SSIM↑	LPIPS↓	PSNR↑	SSIM↑	LPIPS↓	PSNR↑	SSIM↑	LPIPS↓	PSNR↑	SSIM↑	LPIPS↓	PSNR↑	SSIM↑	LPIPS↓	PSNR↑	SSIM↑	LPIPS↓	PSNR↑	SSIM↑	LPIPS↓	PSNR↑	SSIM↑	LPIPS↓
DINOv2	19.77	.7345	.2226	19.04	.7133	.2254	19.91	.7163	.2637	19.47	.7293	.3288	18.00	.6805	.3223	19.27	.7317	.3479	19.42	.6524	.3698	17.64	.5701	.3754	19.21	.6535	.4023
CLIP	19.78	.7378	.2221	19.02	.7113	.2276	19.74	.7136	.2822	19.53	.7295	.3304	18.05	.6771	.3235	19.22	.7310	.3563	19.21	.6552	.3719	17.46	.5669	.3743	19.05	.6582	.4084
DUSt3R	19.88	.7442	.2123	19.01	.7120	.2262	19.87	.7190	.2691	19.64	.7338	.3196	18.01	.6815	.3219	19.39	.7360	.3458	19.29	.6562	.3580	17.54	.5693	.3750	19.19	.6556	.4050
VGGT	19.85	.7450	.2127	19.05	.7120	.2273	19.86	.7165	.2911	19.65	.7372	.3143	18.05	.6770	.3237	19.38	.7358	.3534	19.36	.6590	.3549	17.47	.5645	.3751	19.23	.6604	.4103
RADIO	19.73	.7402	.2207	19.06	.7101	.2301	19.56	.6999	.3252	19.48	.7313	.3139	18.03	.6748	.3254	19.20	.7316	.3654	19.54	.6545	.3465	17.52	.5666	.3748	18.67	.6533	.4216
MASt3R	19.89	.7447	.2123	19.01	.7115	.2261	19.99	.7250	.2657	19.64	.7334	.3188	18.07	.6813	.3211	19.41	.7373	.3464	19.30	.6550	.3576	17.59	.5708	.3722	19.37	.6588	.4027
Ours	19.52	.7457	.2073	18.79	.7140	.2201	19.71	.7199	.2785	18.32	.7085	.3382	17.29	.6626	.3350	18.15	.7147	.3603	19.80	.6643	.3449	17.81	.5850	.3559	19.18	.6693	.3955

	MipNeRF360									**MVImgNet**									**Tanks and Temples**								
	Geometry			Texture			All			Geometry			Texture			All			Geometry			Texture			All		
Feature	PSNR↑	SSIM↑	LPIPS↓	PSNR↑	SSIM↑	LPIPS↓	PSNR↑	SSIM↑	LPIPS↓	PSNR↑	SSIM↑	LPIPS↓	PSNR↑	SSIM↑	LPIPS↓	PSNR↑	SSIM↑	LPIPS↓	PSNR↑	SSIM↑	LPIPS↓	PSNR↑	SSIM↑	LPIPS↓	PSNR↑	SSIM↑	LPIPS↓
DINOv2	20.81	.4946	.3953	19.05	.4495	.3821	20.75	.4924	.4684	19.35	.5896	.3246	16.88	.5359	.3344	19.43	.5943	.3674	18.71	.6432	.3772	17.58	.6214	.3348	18.43	.6443	.4064
CLIP	20.80	.4982	.3913	19.28	.4543	.3807	20.88	.4984	.4773	19.41	.5945	.3098	16.96	.5362	.3358	19.37	.5969	.3695	18.92	.6463	.3729	17.81	.6226	.3316	18.75	.6515	.4052
DUSt3R	20.82	.5008	.3795	19.10	.4489	.3816	21.02	.5048	.4752	19.47	.6004	.3073	16.88	.5348	.3334	19.43	.5937	.3674	18.85	.6458	.3715	17.53	.6222	.3328	18.61	.6477	.4023
VGGT	20.93	.5120	.3639	19.25	.4497	.3828	21.17	.5102	.4892	19.48	.6019	.2975	17.00	.5373	.3346	19.58	.5987	.3748	19.21	.6615	.3547	17.75	.6221	.3319	19.04	.6593	.4017
RADIO	20.87	.5100	.3620	19.35	.4550	.3819	20.91	.5067	.5127	19.54	.6105	.2949	16.99	.5373	.3366	19.60	.5955	.3946	19.19	.6612	.3480	17.84	.6225	.3321	19.01	.6574	.4109
MASt3R	20.92	.5093	.3745	19.21	.4540	.3803	20.92	.5054	.4749	19.49	.6008	.3032	16.91	.5350	.3337	19.49	.5983	.3637	18.80	.6428	.3703	17.68	.6238	.3319	18.76	.6512	.3991
Ours	21.28	.5337	.3562	19.72	.4848	.3595	21.31	.5264	.4698	19.64	.6107	.2942	17.11	.5388	.3313	19.68	.6007	.3774	19.17	.6600	.3577	17.93	.6324	.3248	18.93	.6602	.3970

Table 5: **Per-dataset results of novel view synthesis metrics on Feat2GS benchmark.** Results indicate that our encoder leads to the best performance on most datasets in Geometry, Texture, and All probing modes. The highest, second-highest, and third-highest scores in each category are highlighted with light red , light orange , and light yellow , respectively.

A.3 More experimental results

A.3.1 Evaluation of the geometric-semantic encoder

Evaluation on Feat2GS benchmark We provide comprehensive and detailed results on Feat2GS benchmark (Chen et al., 2024g), as shown in Tab. 5. Results indicate that our encoder leads to the best performance on most datasets in Geometry, Texture, and All probing modes.

Single-frame and video depth estimation Following MonST3R (Zhang et al., 2024), we evaluate single-frame depth on the NYU-v2 (Silberman et al., 2012) dataset and video depth on the BONN (Silberman et al., 2012) dataset, which cover dynamic and static scenes. These datasets are excluded from training, enabling zero-shot performance evaluation across domains. Our evaluation metrics include absolute relative error (Abs Rel) and percentage of predicted depths within a 1.25-factor of true depth (δ < 1.25). Following (Wang et al., 2024b), single-frame evaluation adopts per-frame median scaling, and video evaluation aligns a single scale and/or shift factor per sequence.

We compared our methods with DUSt3R (Wang et al., 2024b), MASt3R (Leroy et al., 2024), Spann3R (Wang & Agapito, 2024), and MonST3R, where these baselines are specially designed for 3D tasks. As shown in Tab. 6 (left), our method achieves competitive results compared to baselines, and even outperforms MASt3R in both single-frame and video depth evaluation.

Method	NYU-v2 (Single-frame)		BONN (Video)	
	Abs Rel ↓	$\delta < 1.25$ ↑	Abs Rel ↓	$\delta < 1.25$ ↑
DUSt3R	0.080	90.7	0.155	83.3
MonST3R	0.102	88.0	**0.067**	**96.3**
Spann3R	0.122	84.9	0.144	81.3
MASt3R	0.129	84.9	0.252	70.1
Ours	**0.070**	**93.9**	0.086	91.4

Method	Params	ImageNet1K		Segmentation	
	(M)	Zero-shot	k-NN	ADE20k	VOC
SAM-H/16	637	-	22.12	28.08	34.34
OpenAI CLIP-L/14	305	75.54	79.96	36.51	67.04
SigLIP-L/14	428	**82.61**	**85.16**	40.53	70.31
DINOv2-g/14-reg	1,137	-	83.41	48.68	82.78
DUSt3R Enc.	303	-	-	32.10	46.02
DUNE-B/14-448	420	-	-	45.60	-
MASt3R Enc.	303	-	-	32.54	48.58
∗RADIOv2.5-L	320	80.55	83.16	**50.68**	**85.60**
UniUGG Enc. (Ours)	320	80.06	83.13	50.12	85.43

Table 6: ***Left:*** **Depth evaluation results.** We report single-frame depth evaluation performance on the NYU-v2 dataset and video depth evaluation performance on the BONN dataset. ***Right:*** **Comparison of encoder performance on the image/pixel level.** 'Zero-Shot' and k-NN are computed on ImageNet-1K. ADE20K and PascalVOC2012 refer to linear probe semantic segmentation mIOU. ∗denotes teachers used to pretrain our encoder.

Method	Params	VSI-Bench								SPAR		
	(M)	Count	Obj.Size	Room	Rel.Dir.	Rel.Dist.	Route	Order	**Avg.**	Low	Medium	High
Qwen25-ViT	669	58.00	51.12	31.04	37.31	29.44	25.26	21.20	35.56	36.50	36.67	39.89
OpenAI CLIP-L/14	305	61.43	49.30	49.31	39.45	**36.20**	30.93	16.18	40.08	44.13	43.67	**52.33**
SigLIP-L/16	316	11.93	42.06	0.73	38.95	27.89	28.87	9.71	23.81	41.75	34.67	43.11
MASt3R Encoder	303	58.12	39.81	48.82	**43.70**	33.24	32.47	19.58	39.14	50.00	42.33	48.22
RADIOv2.5-L	320	59.91	**53.49**	**50.17**	37.08	32.54	30.41	16.18	39.75	50.44	47.95	52.13
UniUGG Enc. (Ours)	320	**62.69**	51.70	49.34	42.14	34.37	**32.99**	**27.51**	**42.18**	**50.82**	**49.07**	51.89

Method	Params	BLINK									Seed-I	Real World
	(M)	Fun.Corr.	Vis.Corr.	Local.	Jigsaw	Depth	Spatial	Simi.	Art	**Avg.**		
Qwen25-ViT	669	15.38	26.16	54.92	46.67	44.35	52.45	46.67	52.99	37.87	41.81	44.97
OpenAI CLIP-L/14	305	24.62	24.42	52.46	**56.00**	45.97	63.64	43.70	52.99	40.45	69.14	54.38
SigLIP-L/16	316	20.00	20.35	**61.48**	51.33	46.77	53.85	**53.33**	56.41	39.08	56.31	45.23
MASt3R Encoder	303	22.31	27.33	55.74	48.67	44.35	67.13	44.44	45.30	40.93	56.96	50.07
RADIOv2.5-L	320	23.08	31.98	47.54	43.33	68.55	65.53	47.31	53.85	42.92	**72.09**	57.38
UniUGG Enc. (Ours)	320	**33.85**	**33.14**	55.74	48.67	**69.35**	**67.83**	51.11	**59.85**	**44.40**	71.65	**58.56**

Table 7: **Detailed comparison results of encoder performance on downstream vision-language reasoning benchmarks.** The VLM architecture is based on Qwen2.5-3B-Instruct, and all encoders are trained under the same settings to ensure fairness.

Image/pixel level evaluation To assess the performance of our encoders, we adopt a set of representative metrics following (Ranzinger et al., 2024b). For image-level reasoning, we evaluate our encoder using Top-1 k-NN accuracy and zero-shot accuracy on the ImageNet-1K dataset (Deng et al., 2009). The zero-shot accuracy is computed using the CLIP language model (Radford et al., 2021). For the k-NN evaluation, we first extract the summary feature for all training images. Then, for each validation image, we identify the *k* nearest neighbors in the feature space and predict the label based on a weighted vote of these neighbors. We also evaluate the generalization performance of our encoder on pixel-level visual tasks, including segmentation mIOU on ADE20k (Zhou et al., 2019) and PascalVOC2012 (Everingham et al., 2015) datasets.

The encoders compared include SAM-H/16 (Kirillov et al., 2023), OpenAI CLIP-L/14 (Radford et al., 2021), SigLIP-L/14 (Zhai et al., 2023) , DINOv2-g/14-reg (Darcet et al., 2023), DUSt3R encoder (Wang et al., 2024b),DUNE-B/14-448 (Sarıyıldız et al., 2025) ,MASt3R encoder (Leroy et al., 2024) and RADIOv2.5-L (Ranzinger et al., 2024b).

Following (Ranzinger et al., 2024b), we freeze the vision encoders and train a linear head on top of the frozen features. The linear probe is conducted in the MMSeg (Contributors, 2020) framework. We train the linear head for 20k steps using a total batch size of 64, a base learning rate of $5e^{-3}$, and the Adam-W optimizer.

As shown in Tab. 6 (right), while our method does not outperform the teacher baseline, it yields competitive results that validate the potential of our encoder. More importantly, it establishes a strong foundation for unified spatial reasoning and 3D generation.

Method	3DSRBench					VSI-Bench								
	Height	Loc.	Orient.	Multi.	**Avg.**	Obj.Count	Abs.Dist.	Obj.Size	RoomSize	Rel.Dist	Rel.Dir.	RoutePlan	Appr.Order	**Avg.**
LLaVA-v1.5-7B	39.1	46.9	28.7	34.7	38.1	6.2	4.9	32.6	2.7	29.6	30.7	26.3	10.5	18.0
LLaVA-NeXT-7B	50.6	59.9	36.1	43.4	48.4	7.5	8.8	27.7	25.8	33.2	29.7	23.7	8.6	20.6
InternVL2.5-8B	45.9	**68.1**	38.7	43.3	50.9	7.7	32.6	42.9	34.6	**39.6**	40.0	24.7	**37.7**	32.5
Qwen2.5-VL-7B	44.1	62.7	40.6	40.5	48.4	26.7	10.8	35.4	31.0	35.2	38.2	**35.1**	29.6	30.3
GPT-4o	**53.2**	59.6	21.6	39.0	44.2	46.2	5.3	43.8	38.2	37.0	**41.3**	31.5	28.5	34.0
UniUGG-3B (Ours)	52.3	60.0	**43.4**	**49.3**	**52.1**	**63.2**	**34.8**	**49.1**	**50.4**	30.3	38.6	26.3	26.7	**40.1**

Table 8: **Detailed spatial understanding scores on 3DSRBench and VSI-Bench.** Our *UniUGG* is jointly trained for both spatial understanding and 3D generation tasks. Note that the LLM used in *UniUGG* has a size of only 3B parameters.

Method	3D	SQA3D	ScanQA		
		EM	BLEU-4	CiDEr	EM
3D-LLM	✓	-	12.0	69.4	20.4
Chat-3D v2	✓	54.7	14.0	87.6	-
LEO	✓	50.0	13.2	101.4	21.5
LL3DA	✓	-	13.5	76.8	-
Scene-LLM	✓	54.2	12.0	80.0	27.2
LLaVA-3D	✓	55.6	14.5	91.7	27.0
Video-3D LLM	✓	**58.6**	**16.2**	**102.1**	**30.1**
UniUGG (Ours)	✗	51.3	12.1	85.6	24.4

Methods	Acc@0.25	Acc@0.5
ScanRefer	37.3	24.3
MVT	40.8	33.3
ViL3DRel	47.9	37.7
3D-LLM	30.3	-
Chat-3D v2	35.9	30.4
Grounded 3D-LLM	47.9	44.1
LLaVA-3D	54.1	42.4
Video-3D LLM	**58.1**	**51.7**
∗*UniUGG* (Ours)	23.2	7.8
UniUGG (Ours)	41.9	36.6

Table 9: ***Left:*Performance comparison on SQA3D and ScanQA.** "3D" indicates whether the model is infused with 3D information. ***Right:*Performance comparison across different models on ScanRefer.** ∗indicates results without refine.

Downstream task performance As shown in Tab. 7, we provide more detailed results about *Tab. 2 of the main text*. Our encoder (*UniUGG* Enc.) demonstrates clear advantages on spatial reasoning tasks and two general QA benchmarks. It shows that our encoder has more consistent performance across modalities, balancing spatial perception and high-level semantics.

A.3.2 Evaluation of spatial understanding

Detailed spatial understanding scores As shown in Tab. 8, we present more fine-grained spatial understanding scores on 3DSRBench and VSI-Bench (corresponding to *Tab. 3 of the main text*). We jointly train *UniUGG* for both spatial understanding and 3D generation tasks. The model utilizes our pretrained geometric-semantic encoder as the visual backbone and employs Qwen2.5-3B-Instruct as the large language model. The results demonstrate that *UniUGG* can capture precise spatial relations by jointly modeling 3D structure and visual-language reasoning. It should be noted that the LLM used in *UniUGG* has a size of only 3B parameters.

Evaluation on 3D-specific benchmarks We further evaluate the 3D reasoning capability of our *UniUGG* on SQA3D (Ma et al., 2022), ScanQA (Azuma et al., 2022), and ScanRefer (Chen et al., 2020), which are widely adopted benchmarks in 3D VLMs. Due to the differences in QA formats, and following the practice of prior works, we apply supervised fine-tuning on 3D tasks to better assess *UniUGG*'s spatial capabilities. First, we evaluate spatial understanding using SQA3D and ScanQA, which focus on object attributes, spatial relations, and viewpoint-conditioned reasoning. Compared models include 3D-LLM (Hong et al., 2023), Chat-3D v2 (Huang et al., 2023a), LEO (Huang et al., 2023b), LL3DA (Chen et al., 2024e), Scene-LLM (Fu et al., 2024a), LLaVA-3D (Zhu et al., 2024a) and Video-3D LLM (Zheng et al., 2024). As shown in Tab. 9 (left), although our model does not incorporate explicit 3D information, it achieves competitive performance compared to 3D-enhanced LLMs. Additionally, we assess 3D grounding on the ScanRefer dataset, where the task requires localizing target objects based on textual descriptions. Compared models include ScanRefer, MVT (Huang et al., 2022), ViL3DRel Chen et al. (2022), 3D-LLM, Chat-3D v2, Grounded 3D-LLM Chen et al. (2024f), LLaVA-3D, and Video-3D LLM. As shown in Tab. 9 (right), our model may struggle to predict depth accurately due to the absence of 3D information, resulting in poor grounding results. To address this, we apply a refinement strategy to mitigate this issue and improve grounding performance. These results highlight the potential of our *UniUGG* to perform spatial reasoning and grounding without relying on explicit 3D inputs, while still supporting more complex

Method	VSI	BLINK	3DSR	SPAR
UniUGG (full)	40.1	43.6	**52.1**	47.2
UniUGG (und. only)	**42.2**	**44.4**	51.3	**49.8**

Method	ARKitScenes			ScanNet++		
	FID↓	KID↓	LPIPS↓	FID↓	KID↓	LPIPS↓
UniUGG (full)	55.01	.0425	.4849	55.64	**.0442**	.4263
UniUGG (gen. only)	**54.35**	**.0409**	**.4556**	**55.46**	.0454	**.3586**

Table 10: **Performance comparison with separate optimization.**

generative tasks. It should be noted that our model employs a backbone with 3B parameters, while other methods, for example, LLaVA-3D and Video-3D-LLM, use 7B-parameter backbones.

A.3.3 Evaluation of 3D generation

More qualitative results of 3D generation We provide more visualization results to further demonstrate the 3D generation and understanding capabilities of *UniUGG*. Given a reference image, we randomly sample plausible relative view transformations and let *UniUGG* generate the corresponding 3D scenes. *UniUGG* further captioned the generated 3D scenes. As shown in Fig. 7, Fig. 8, Fig. 9, and Fig. 10, *UniUGG* consistently produces geometrically coherent and semantically meaningful 3D content, along with accurate scene captions.

Feature matching visualization By taking only a reference image and the relative view transformation as input, *UniUGG* predicts the ViT tokens of the target image, which, together with the reference tokens, are then decoded into point clouds and the corresponding cross-view feature matchings. We visualize these feature matching results in Fig. 11 and compare them with the baseline method MASt3R (Leroy et al., 2024), which requires both the reference and ground-truth transformed-view images as input to obtain feature matching. Our method achieves highly accurate feature matching, which is highly consistent with those produced by MASt3R. This demonstrates that *UniUGG* not only generates the spatial structure under the novel view but also ensures that the generated content is generally consistent with the input view transformation condition.

Robust generation under extreme view transformation We illustrate the generation performance of *UniUGG* under extreme view transformation conditions, as shown in Fig. 12. We evaluate the model performance conditioned on rotation angles of 60°, 80°, 100°, 120°, and 140°. As observed, within the range of 60°-120°, *UniUGG* still produces high-quality, semantically rich, and structurally coherent 3D point clouds. However, at 140° or beyond, the generation quality drops noticeably, with the point clouds exhibiting blurred textures and distorted structures. This degradation arises from two factors. First, during training, the view-transformation conditions are usually constrained within: view overlap ratio > 0.4, rel-translation < 2 m, and rel-rotation < 120°. Consequently, when evaluated under extreme view transformation (e.g., rotation > 140°), our model struggles to maintain generation quality. Second, such large viewpoint changes significantly reduce the overlap between the reference and target images, resulting in insufficient cross-view constraints and finally leading to failures in 3D generation.

Failure case Due to the lack of training samples with large view transformations, *UniUGG* would generate point clouds with blurred textures and distorted structure under extreme viewpoint changes, as shown in Fig. 12. What's more, we also provide some examples of failure cases in Fig. 13. In some cases, *UniUGG* generates point clouds with color distortions, where vivid green regions are mistakenly inferred as grayish colors. This may be caused by a conflict between color decoding and semantic representation tasks during encoder pretraining.

A.3.4 Performance of separately optimized

As shown in Tab. 10, we separately optimize the spatial understanding task and the 3D generation task, and compare their performance with that of the jointly trained model. Benefiting from the Spatial-VAE and diffusion model, joint training (*UniUGG* full) does not significantly degrade the performance of 3D generation (*UniUGG* gen. only) and only leads to a moderate reduction in spatial understanding (*UniUGG* und. only) performance. We believe this performance trade-off is acceptable: although a small amount of understanding performance is sacrificed, we obtain a unified 3D model for both understanding and generation. This unification substantially reduces training cost and computational overhead while broadening the range of tasks the model can support.

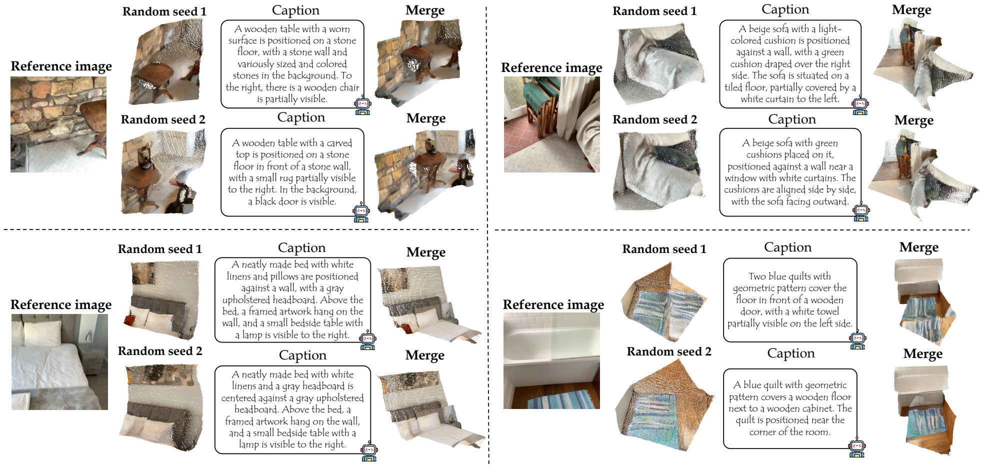

A wooden table with a worn surface is positioned on a stone floor, with a stone wall and variously sized and colored stones in the background. To the right, there is a wooden chair is partially visible.

A wooden table with a carved top is positioned on a stone floor in front of a stone wall, with a small rug partially visible to the right. In the background, a black door is visible.

A beige sofa with a light-colored cushion is positioned against a wall, with a green cushion draped over the right side. The sofa is situated on a tiled floor, partially covered by a white curtain to the left.

A beige sofa with green cushions placed on it, positioned against a wall near a window with white curtains. The cushions are aligned side by side, with the sofa facing outward.

A neatly made bed with white linens and pillows are positioned against a wall, with a gray upholstered headboard. Above the bed, a framed artwork hang on the wall, and a small bedside table with a lamp is visible to the right.

A neatly made bed with white linens and a gray headboard is centered against a gray upholstered headboard. Above the bed, a framed artwork hang on the wall, and a small bedside table with a lamp is visible to the right.

Two blue quilts with geometric pattern cover the floor in front of a wooden door, with a white towel partially visible on the left side.

A blue quilt with geometric pattern covers a wooden floor next to a wooden cabinet. The quilt is positioned near the corner of the room.

Figure 7: **Additional visualization samples.** We present 3D scene generations and the corresponding captions produced by our *UniUGG* under varying random seeds.

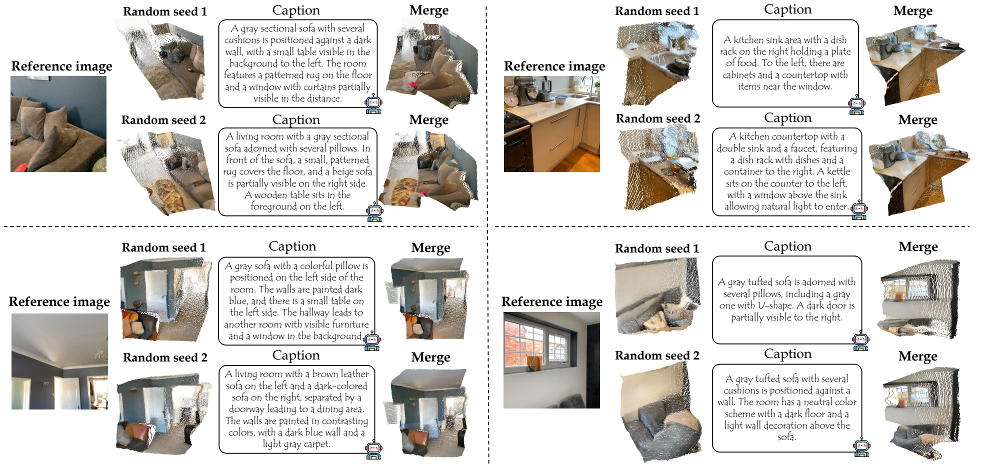

A gray sectional sofa with several cushions is positioned against a dark wall, with a small table visible in the background to the left. The room features a patterned rug on the floor and a window with curtains partially visible in the distance.

A living room with a gray sectional sofa adorned with several pillows. In front of the sofa, a small, patterned rug covers the floor, and a beige sofa is partially visible on the right side. A wooden table sits in the foreground on the left.

A kitchen sink area with a dish rack on the right holding a plate of food. To the left, there are cabinets and a countertop with items near the window.

A kitchen countertop with a double sink and a faucet, featuring a dish rack with dishes and a container to the right. A kettle sits on the counter to the left, with a window above the sink allowing natural light to enter.

A gray sofa with a colorful pillow is positioned on the left side of the room. The walls are painted dark blue, and there is a small table on the left side. The hallway leads to another room with visible furniture and a window in the background.

A living room with a brown leather sofa on the left and a dark-colored sofa on the right, separated by a doorway leading to a dining area. The walls are painted in contrasting colors, with a dark blue wall and a light gray carpet.

A gray tufted sofa is adorned with several pillows, including a gray one with U-shape. A dark door is partially visible to the right.

A gray tufted sofa with several cushions is positioned against a wall. The room has a neutral color scheme with a dark floor and a light wall decoration above the sofa.

Figure 8: **Additional visualization samples.** We present 3D scene generations and the corresponding captions produced by our *UniUGG* under varying random seeds.

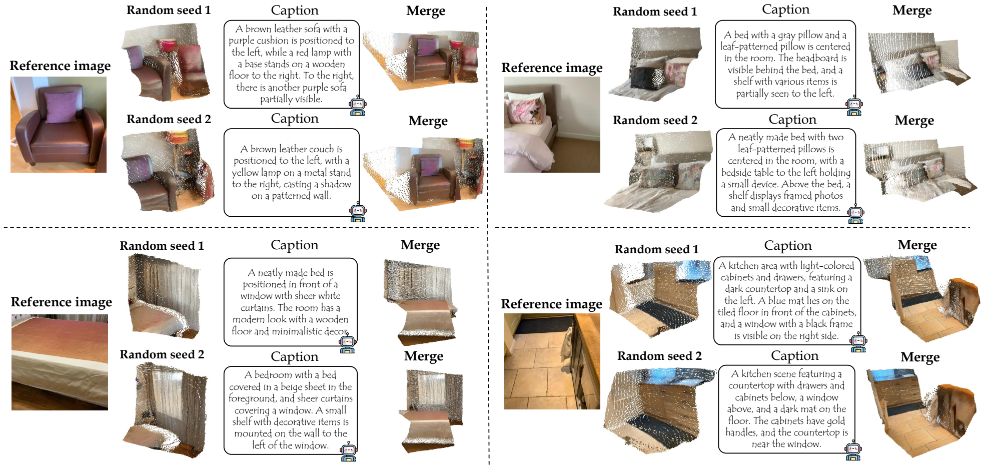

A brown leather sofa with a purple cushion is positioned to the left, while a red lamp with a base stands on a wooden floor to the right. To the right, there is another purple sofa partially visible.

A brown leather couch is positioned to the left, with a yellow lamp on a metal stand to the right, casting a shadow on a patterned wall.

A bed with a gray pillow and a leaf-patterned pillow is centered in the room. The headboard is visible behind the bed, and a shelf with various items is partially seen to the left.

A neatly made bed with two leaf-patterned pillows is centered in the room, with a bedside table to the left holding a small device. Above the bed, a shelf displays framed photos and small decorative items.

A neatly made bed is positioned in front of a window with sheer white curtains. The room has a modern look with a wooden floor and minimalistic decor.

A bedroom with a bed covered in a beige sheet in the foreground, and sheer curtains covering a window. A small shelf with decorative items is mounted on the wall to the left of the window.

A kitchen area with light-colored cabinets and drawers, featuring a dark countertop and a sink on the left. A blue mat lies on the tiled floor in front of the cabinets, and a window with a black frame is visible on the right side.

A kitchen scene featuring a countertop with drawers and cabinets below, a window above, and a dark mat on the floor. The cabinets have gold handles, and the countertop is near the window.

Figure 9: **Additional visualization samples.** We present 3D scene generations and the corresponding captions produced by our *UniUGG* under varying random seeds.

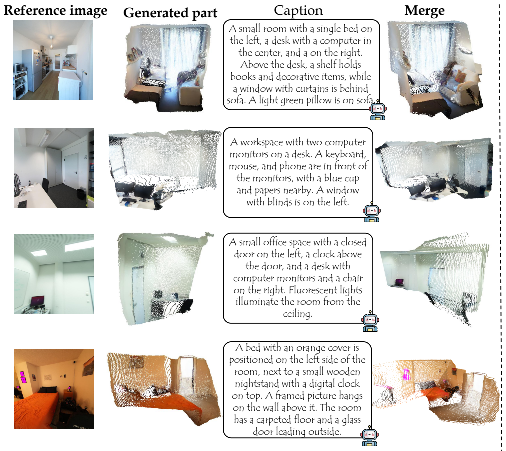

A small room with a single bed on the left, a desk with a computer in the center, and a on the right. Above the desk, a shelf holds books and decorative items, while a window with curtains is behind sofa. A light green pillow is on sofa.

A workspace with two computer monitors on a desk. A keyboard, mouse, and phone are in front of the monitors, with a blue cup and papers nearby. A window with blinds is on the left.

A small office space with a closed door on the left, a clock above the door, and a desk with computer monitors and a chair on the right. Fluorescent lights illuminate the room from the ceiling.

A bed with an orange cover is positioned on the left side of the room, next to a small wooden nightstand with a digital clock on top. A framed picture hangs on the wall above it. The room has a carpeted floor and a glass door leading outside.

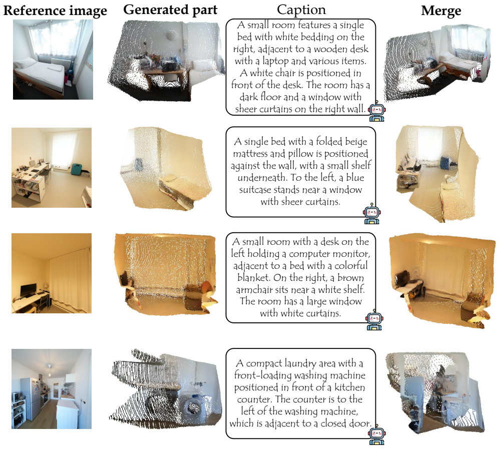

A small room features a single bed with white bedding on the right, adjacent to a wooden desk with a laptop and various items. A white chair is positioned in front of the desk. The room has a dark floor and a window with sheer curtains on the right wall.

A single bed with a folded beige mattress and pillow is positioned against the wall, with a small shelf underneath. To the left, a blue suitcase stands near a window with sheer curtains.

A small room with a desk on the left holding a computer monitor, adjacent to a bed with a colorful blanket. On the right, a brown armchair sits near a white shelf. The room has a large window with white curtains.

A compact laundry area with a front-loading washing machine positioned in front of a kitchen counter. The counter is to the left of the washing machine, which is adjacent to a closed door.

Figure 10: **Additional visualization samples.** We present 3D scene generations and the corresponding captions produced by our *UniUGG*.

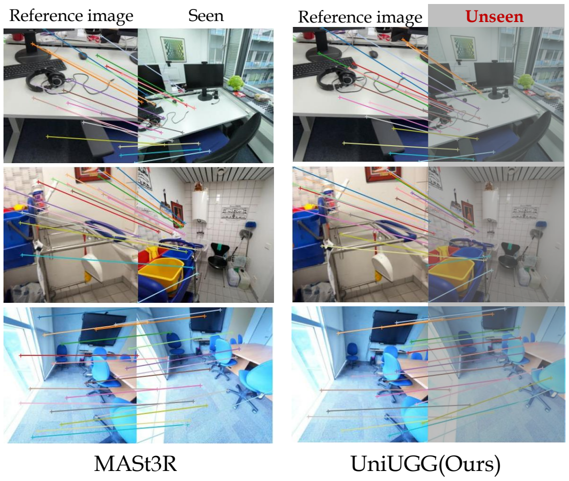

Figure 11: **Feature matching visualization.** Without access to the target image, our method takes the reference image and the relative view transformation as input and still produces accurate feature matchings, while baseline MASt3R takes image pairs as input.

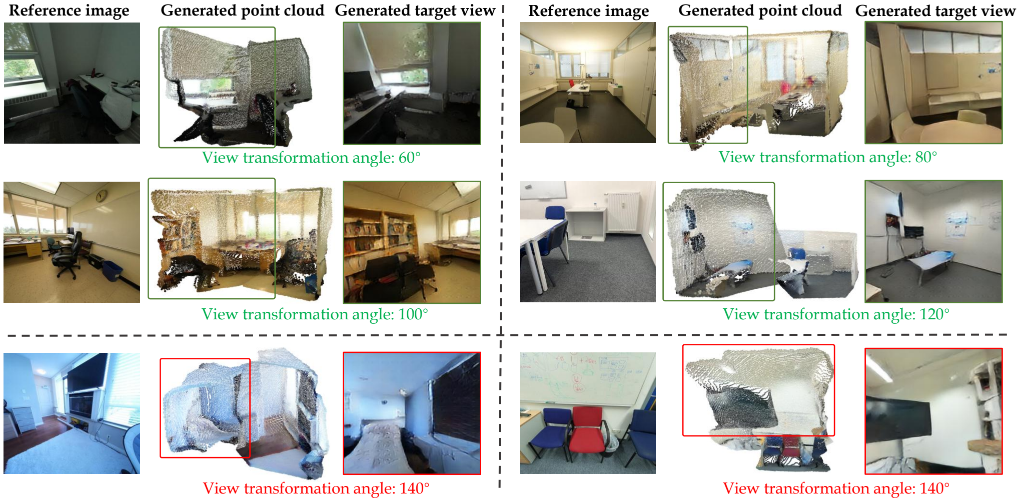
Reference image
Generated point cloud
Generated target view
Reference image
Generated point cloud
Generated target view
View transformation angle: 60°
View transformation angle: 80°
View transformation angle: 100°
View transformation angle: 120°
View transformation angle: 140°
View transformation angle: 140°

Figure 12: **3D generation under extreme view transformation.** When the rotation angle is below 120°, *UniUGG* can still produce high-quality 3D point clouds under the target viewpoint. As the rotation angle increases to 140° or beyond, the quality of the generated results degrades noticeably.

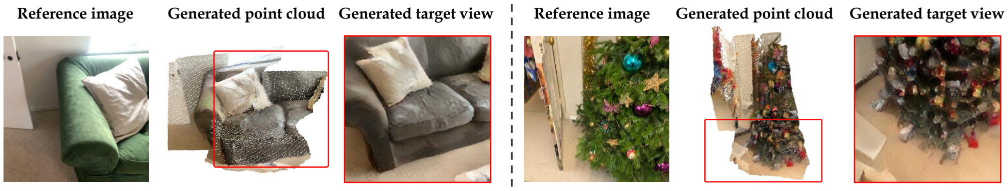

Figure 13: Other failure cases of our model.

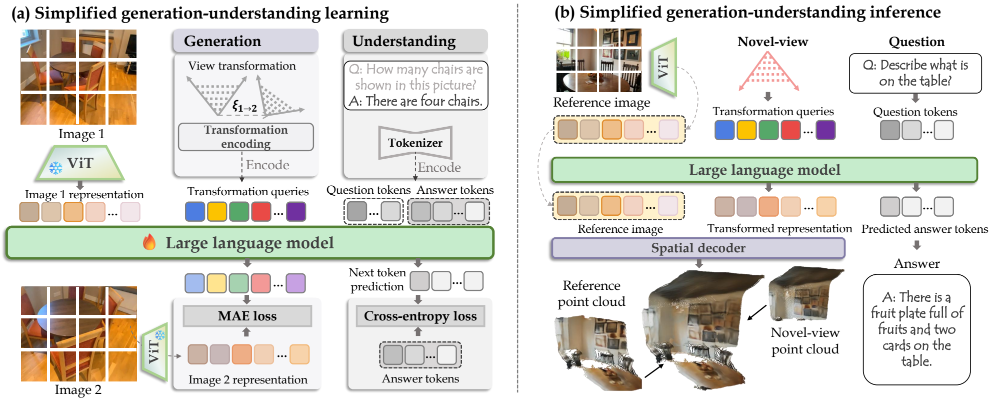

Figure 14: **Overview of our simplified model variant pipeline.** In the simplified variant, we do not use the diffusion model and Spatial-VAE for scene generation but directly produce the novel-view tokens by LLM, which is supervised with ground truth tokens.

A.4 Exploration of simplified model variant

During the development of our proposed *UniUGG*, we explored the early or simplified version of the model architecture. This helped us better understand the role of the core component in the model. Although not intended as the final model, the simplified variant provides valuable insights for designing a unified framework for 3D understanding and generation.

As shown in Fig 14 (a), during training, LLM learns both spatial generation capability across views by predicting ViT tokens of the novel view, and visual understanding capability via question answering As shown in Fig 14 (b), at inference, the model performs either novel-view spatial generation or question answering using a single image as reference, conditioned on the input type.

We present visualization generation results of the simplified variant in Fig. 15. While it outperforms the baseline CUT3R in terms of generating fine-grained spatial structures, its textures remain noticeably inferior to those of our full *UniUGG*. This performance gap is primarily attributed to the absence of the diffusion prior and Spatial-VAE, which play a crucial role in modeling high-frequency visual details and realistic textures. The simplified variant, lacking these core components, tends to generate over-smoothed surfaces.

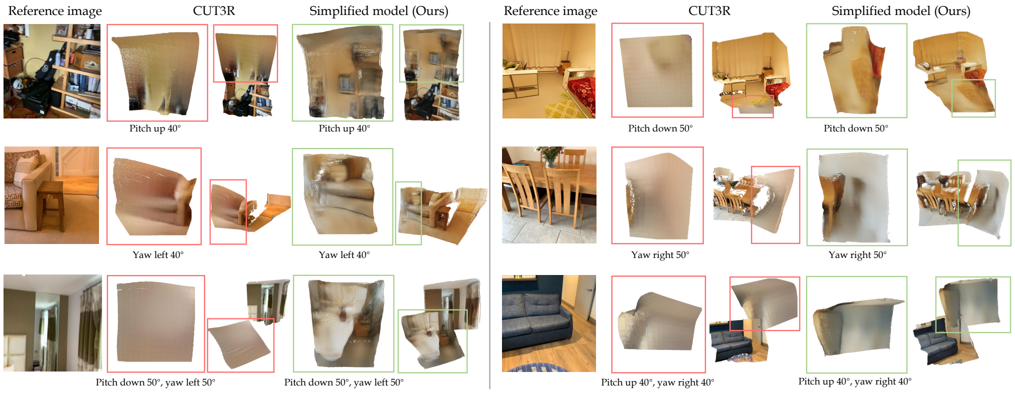

Figure 15: **Visualization of scenes generated by the simplified model variant.** Although the simplified variant can imagine spatial structures under novel views, it lacks clear details.